

Propane Dehydrogenation Catalyzed by Isolated Pt Atoms in $\equiv\text{SiOZn}-\text{OH}$ Nests in Dealuminated Zeolite Beta

Liang Qi, Melike Babucci, Yanfei Zhang, Alicia Lund, Lingmei Liu, Jingwei Li, Yizhen Chen, Adam S. Hoffman, Simon R. Bare, Yu Han, Bruce C. Gates, and Alexis T. Bell*

Cite This: *J. Am. Chem. Soc.* 2021, 143, 21364–21378

Read Online

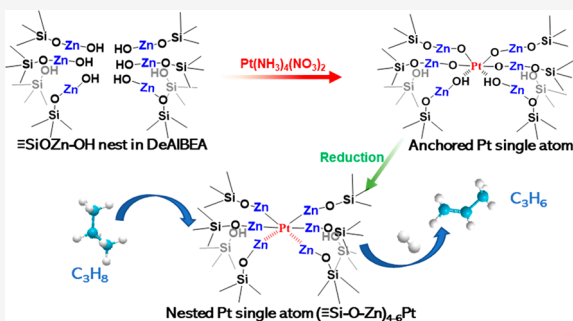
ACCESS |

Metrics & More

Article Recommendations

Supporting Information

ABSTRACT: Atomically dispersed noble metal catalysts have drawn wide attention as candidates to replace supported metal clusters and metal nanoparticles. Atomic dispersion can offer unique chemical properties as well as maximum utilization of the expensive metals. Addition of a second metal has been found to help reduce the size of Pt ensembles in bimetallic clusters; however, the stabilization of isolated Pt atoms in small nests of nonprecious metal atoms remains challenging. We now report a novel strategy for the design, synthesis, and characterization of a zeolite-supported propane dehydrogenation catalyst that incorporates predominantly isolated Pt atoms stably bonded within nests of Zn atoms located within the nanoscale pores of dealuminated zeolite Beta. The catalyst is stable in long-term operation and exhibits high activity and high selectivity to propene. Atomic resolution images, bolstered by X-ray absorption spectra, demonstrate predominantly atomic dispersion of the Pt in the nests and, with complementary infrared and nuclear magnetic resonance spectra, determine a structural model of the nested Pt.



INTRODUCTION

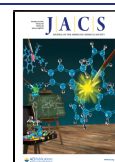
Thermal dehydrogenation of propane (PDH), derived from shale gas, is an attractive source of propene for manufacturing polypropylene, propene oxide, acrylic acid, and acrylonitrile.^{1–6} Current world demand for propene is rising at 6% per annum.⁷ Pt is the metal of choice as an industrial PDH catalyst because it exhibits high activity for C–H bond activation and relatively low activity for the undesired C–C bond cleavage.^{4,8–19} However, supported monometallic Pt clusters undergo rapid deactivation caused by coke formation and sintering at the high temperatures (>773 K) required for this endergonic reaction.^{6,8,20} Cluster size affects all aspects of the performance of Pt for PDH.^{15,17,18,20–23} As Pt dispersion increases from 2 nm clusters to single atoms, the turnover frequency (TOF) for propane consumption increases, as does the propene selectivity, and catalyst stability parallels propene selectivity.²¹ Incorporation of other elements (e.g., Cu,²⁴ Zn,^{8,10,14} Fe,²⁵ Ga,²⁶ In,²⁷ Sn,^{1,11,20} Mn,²⁸ Co,²⁹ and La⁴) reduces the size of Pt ensembles on the bimetallic Pt cluster surfaces. Both the reduction in Pt cluster size and the addition of a second metal reduce the activation barrier for propene desorption relative to that for further dehydrogenation, which is undesired because it leads ultimately to coke formation and catalyst deactivation.^{16,30} This benefit is strongest for isolated Pt atoms which exhibit a slight positive charge²¹ and for additive metals that lower the d-band center of the metal of small Pt clusters (e.g., Sn and In); however, in the latter case this beneficial effect is offset by a loss in specific activity.^{16,30} An

alternative approach to achieving high activity, selectivity, and stability is to produce isolated Pt atoms that are stabilized in small nests of nonprecious metal atoms, such as Zn. Although several attempts to do so have been reported,^{8,10,31–33} it remains a challenge to isolate the Pt atoms entirely within nests and to achieve performance characterized by high mass-specific activity, propene selectivity, and strong resistance to sintering and deactivation during PDH. We now report attainment of these goals.

We grafted Zn–OH groups to the individual hydroxyl groups located with the silanol nests of dealuminated zeolite beta (DeAlBEA),³⁴ and the nests of Zn–OH groups that formed were used to anchor Pt atoms. We designate our catalysts as $x\text{Pt}-y\text{Zn}-\text{DeAlBEA}$ (x and y are atomic ratios of an element with respect to the original inventory of Al). These materials were characterized with complementary spectroscopic and microscopic methods to show that Pt is predominantly dispersed atomically as cations with an apparent oxidation state of $\sim +4$. Taken in aggregate, our characterization results suggest that the atomically dispersed Pt is present in complexes anchored to the

Received: September 27, 2021

Published: December 9, 2021



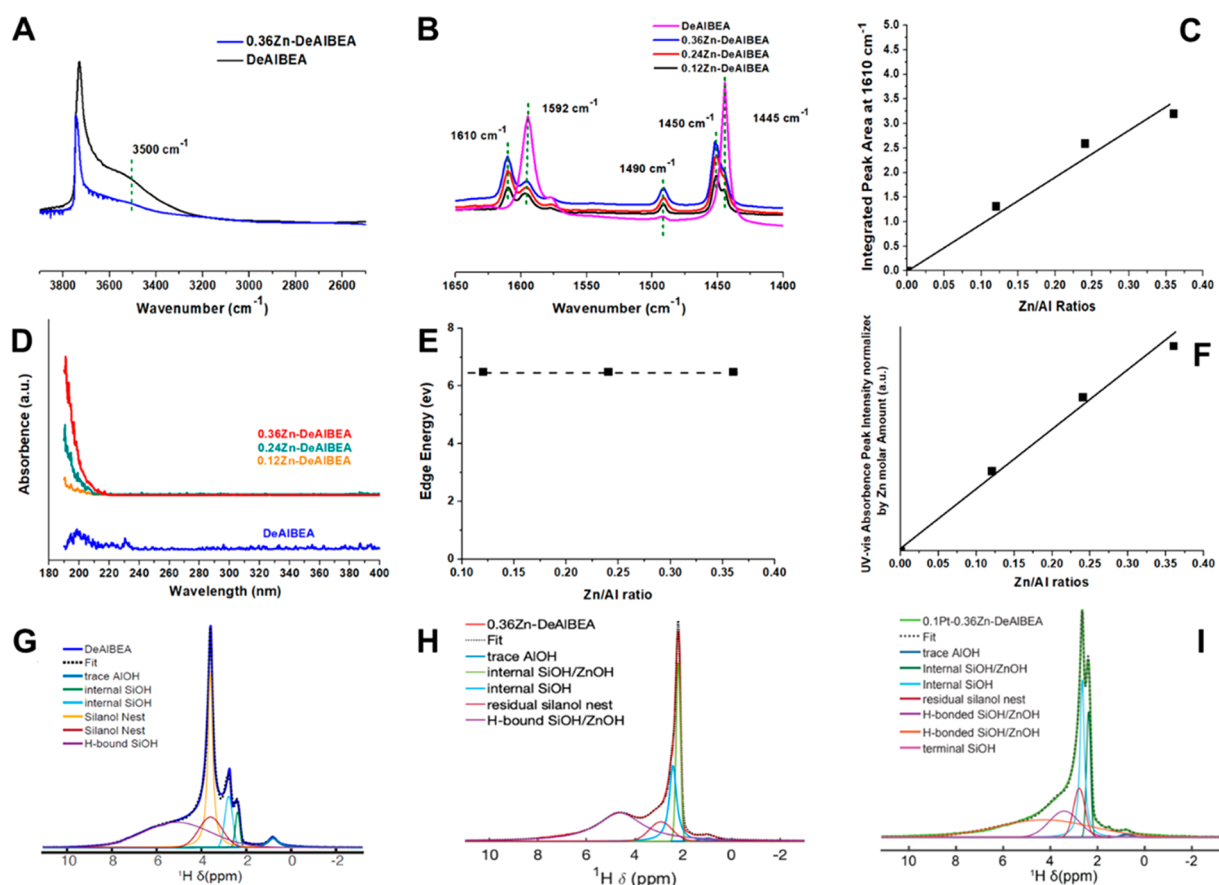


Figure 1. Comparison of hydroxyl stretching region (A) and pyridine-adsorbed FTIR (B) of DeAlBEA and Zn-DeAlBEA. (C) Integration of pyridine-adsorbed FTIR peak signal at 1610 cm^{-1} . (D) UV-vis results characterizing DeAlBEA and Zn-DeAlBEA. (E) UV-vis Zn edge energy characterizing Zn-DeAlBEA samples. (F) UV-vis signal intensity normalized by Zn molar amount. ^1H NMR spectra of (G) DeAlBEA, (H) 0.36Zn-DeAlBEA, and (I) 0.1Pt-0.36Zn-DeAlBEA.

zeolite, which we refer to as $(\equiv\text{Si}-\text{O}-\text{Zn})_{4-6}\text{Pt}$. These structures exhibit an intrinsic PDH activity that is higher than that reported for PtZn-based PDH catalysts and a selectivity and stability that are among the best reported.

RESULTS AND DISCUSSION

Creation of $\equiv\text{SiOZn}-\text{OH}$ Nests in DeAlBEA. ^{27}Al NMR spectra of H-BEA and DeAlBEA indicate essentially complete removal of framework and extra-framework Al upon dealumination (Figure S3A in the Supporting Information);³⁵ consistent with this result, ICP analysis to determine the Al content of H-BEA before dealumination gave a value of 2.54 wt %, with the analysis of the zeolite after dealumination giving a value of 0.01–0.02 wt %, indicating that more than 99.2% of the Al had been removed. However, no changes in the zeolite lattice structure were observed by XRD (Figure S1A). Further indications of changes upon dealumination were obtained by comparison of the IR spectra of the H-BEA and DeAlBEA. Figure S2 in the Supporting Information shows that H-BEA has characteristic bands at 3743 cm^{-1} (isolated silanol), 3606 cm^{-1} (Brønsted acid O–H groups), 3660 cm^{-1} , and 3780 cm^{-1} (Al–OH groups).³⁶ After dealumination, the bands characterizing all Al-related –OH groups disappeared, and a large number of internal silanol groups were created, characterized by bands at 3728 cm^{-1} and a broad, intense absorption characterizing silanol nests, centered at 3500 cm^{-1} .^{34–36} These changes indicate that, upon dealumination, internal silanol groups and silanol nests

were created within the crystalline zeolite framework.³⁴ Additional evidence for dealumination and the formation of silanol nests was obtained from an IR spectrum of adsorbed pyridine on DeAlBEA, presented in Figure S2B in the Supporting Information. Almost all of the bands characterizing pyridine interactions with Brønsted acid (1545 and 1637 cm^{-1}), Lewis acid (1620 and 1455 cm^{-1}), and the combination of Brønsted and Lewis acid (1490 cm^{-1}) sites disappeared following dealumination. Instead, two new bands appeared, at 1592 and 1445 cm^{-1} , that are assigned to the interaction of pyridine with H atoms of the Si–OH groups in the silanol nests in DeAlBEA.³⁵

The method of Zn introduction into DeAlBEA to produce Zn-DeAlBEA is summarized in Experimental Methods. FTIR spectra of Zn-DeAlBEA show that the band characterizing silanol nests at 3500 cm^{-1} of DeAlBEA decreased in intensity (Figure 1A), as did the bands for pyridine hydrogen-bonded with silanol nests, at 1592 and 1445 cm^{-1} (Figure 1B). Concomitantly, two new signals appeared, at 1610 and 1450 cm^{-1} , assigned to pyridine interacting with Zn Lewis acid sites (Figure 1B). The intensities of these peaks increased linearly with the Zn/Al ratio in the range of 0.12–0.36 (Figure 1C).

UV-vis spectra of Zn-DeAlBEA samples (Figure 1D) show that, after grafting of Zn, the broad absorption centered at ca. 200 nm and ascribed to $\equiv\text{Si}-\text{OH}$ groups lost intensity,^{37,38} as a result of the reaction of these groups with Zn. A new absorption signal appeared at ca. 195 nm that is similar to that reported at 195 nm for charge transfer transitions of grafted Zn species with

Table 1. Summary of EXAFS Fit Parameters at Zn K-Edge Characterizing 0.36Zn-DeAlBEA and 0.04Pt-0.36Zn-DeAlBEA after Treatments under Various Conditions^a

sample	scattering path	<i>N</i>	<i>R</i> (Å)	$\Delta\sigma^2 \times 10^3$ (Å ²)	ΔE_0 (eV)	<i>R</i> -factor	reduced χ^2
pretreated 0.36Zn-DeAlBEA (Zn-containing zeolite)	Zn–O _s	2.0 ± 1.0	1.88 ± 0.08	9 ± 5	3.2 ± 3.6	0.02	558
	Zn–Zn	0.8 ± 0.8	2.66 ± 0.10	7 ± 2	–8.9 ± 2.6		
	Zn–(O)–Si	0.8 ± 0.6	3.12 ± 0.11	5 ± 5	3.2 ± 3.6		
as-synthesized 0.04Pt-0.36Zn-DeAlBEA	Zn–O _s	4.3 ± 0.3	1.95 ± 0.01	8 ± 4	0.4 ± 0.9	0.01	131
	Zn–(O)–Si	0.6 ± 0.2	3.15 ± 0.08	4 ± 2	0.4 ± 0.9		
pretreated 0.04Pt-0.36Zn-DeAlBEA	Zn–O _s	1.9 ± 0.2	1.90 ± 0.06	8 ± 4	2.1 ± 1.9	0.02	256
	Zn–Zn	0.6 ± 0.1	2.70 ± 0.04	7 ± 5	–7.2 ± 4.1		
	Zn–(O)–Si	0.5 ± 0.1	3.17 ± 0.06	4 ± 2	2.1 ± 1.9		
postcatalytic reaction 0.04Pt-0.36Zn-DeAlBEA	Zn–O _s	2.2 ± 0.1	1.90 ± 0.06	8 ± 4	0.5 ± 0.8	0.02	301
	Zn–Zn	0.5 ± 0.2	2.68 ± 0.06	7 ± 5	–4.5 ± 2.9		
	Zn–(O)–Si	0.5 ± 0.3	3.17 ± 0.06	4 ± 2	0.5 ± 0.8		

^aThe range in *k* was 3.0–10.0 Å^{–1}, and the fit range in distance *r* was 1.0–3.3 Å. Notation: *N*, coordination number; *R*, scattering path length between the absorber and the scattering atom; $\Delta\sigma^2$, mean square relative displacement; ΔE_0 , inner potential correction. O_s denotes single-scattering Zn–O_s, Zn single-scattering Zn–Zn, and Si single-scattering Zn–(O)–Si.

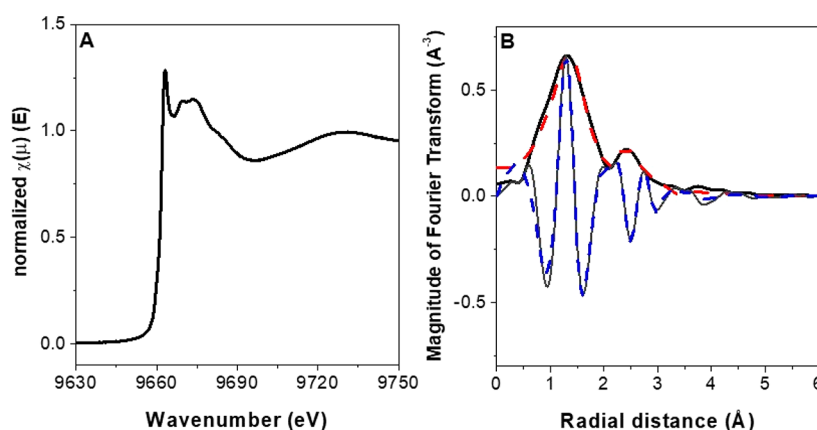


Figure 2. XAS results characterizing 0.36Zn-DeAlBEA after exposure to flowing He at 823 K for 30 min and cooling to 298 K. (A) XANES spectra and (B) Zn K-edge EXAFS data (magnitude of the Fourier transform (FT) (*k*²-weighted)) and results of EXAFS modeling. Imaginary part (solid gray line) and magnitude of the FT (*k*²-weighted) of data (solid black line) and calculated contribution (dashed red line). The range in *k* was 3.0–10.0 Å^{–1}, and the fit range in radial distance was 1.0–3.3 Å.

lattice O^{2–} in a zeolite framework.^{39,40} When the Zn/Al ratio increased to 0.24 and then 0.36, the UV–vis absorption intensity increased relative to that for 0.12Zn-DeAlBEA. For none of the samples was an absorption band observed at 368 nm, consistent with the absence of crystalline ZnO.⁴¹ Further, in agreement with this result, the photon absorption energy attributed to ligand-to-metal charge transfer from O to isolated Zn(II) is estimated to be 6.5 eV for all Zn-DeAlBEA samples (Figure 1E), a value that is much greater than that for bulk ZnO (3.15 eV).⁴² Thus, the UV–vis edge energy data indicate that all the Zn atoms introduced into DeAlBEA were grafted to the zeolite framework and did not generate ZnO_x species, consistent with the FTIR spectra characterizing adsorbed pyridine (Figure 1C).

Of further note, the UV–vis absorption intensity per Zn atom increased linearly with the Zn/Al ratio (Figure 1F), suggesting that, although the Zn atoms were grafted to the zeolite framework, there were nonetheless weak interactions between neighboring Zn sites when the Zn/Al ratio was >0.12. A possible reason for these interactions is that, besides the charge transfer from O atoms of the zeolite framework to Zn atoms (≡Si–O → Zn), the O atoms of ZnOH groups also facilitate charge transfer from O^{2–} to neighboring Zn²⁺ ions (≡SiOZn(HO) → Zn), enhancing the intensity of the UV–vis signal. Therefore, the

UV–vis spectra suggest that the ≡SiOZn–OH species in the ≡SiOZn–OH nests of 0.36Zn-DeAlBEA interact weakly.

The chemical changes occurring after H-BEA dealumination and introduction of Zn were probed using NMR spectroscopy. Creation of hydrogen-bonded ≡Si–OH groups in silanol nests after H-BEA dealumination by nitric acid leaching was confirmed by the ¹H NMR signature (Figure 1G) at 3.6 ppm. Introduction of Zn led to a loss of ≡Si–OH nest groups (peak at 3.6 ppm), consistent with the FTIR results. Moreover, the relative intensities of the peaks at 2.4 and 2.7 ppm (2.8 ppm for DeAlBEA) changed, with the 2.4 ppm signal showing much higher intensity, indicating that the peak at 2.4 ppm is associated with the newly introduced Zn–OH groups. Formation of ≡SiOZn–OH species has been reported to be characterized by a proton chemical shift of approximately 2.4 ppm (Figure 1H).⁴³ The ¹H–²⁹Si cross-polarization (CP) NMR spectrum in Figure S3B,C shows that, upon addition of Zn to the DeAlBEA material, a peak appeared with an isotropic shift of –92.1 ppm and a line width of 5.1 ppm for 0.36Zn-DeAlBEA, which is attributed to the formation of ≡SiOZn–OH (further details are given in the Supporting Information). For reference, we note that the chemical shifts characterizing ≡SiOZn–OH species in various silicate frameworks exhibit a range of values from –88 to –100 ppm.^{44–46}

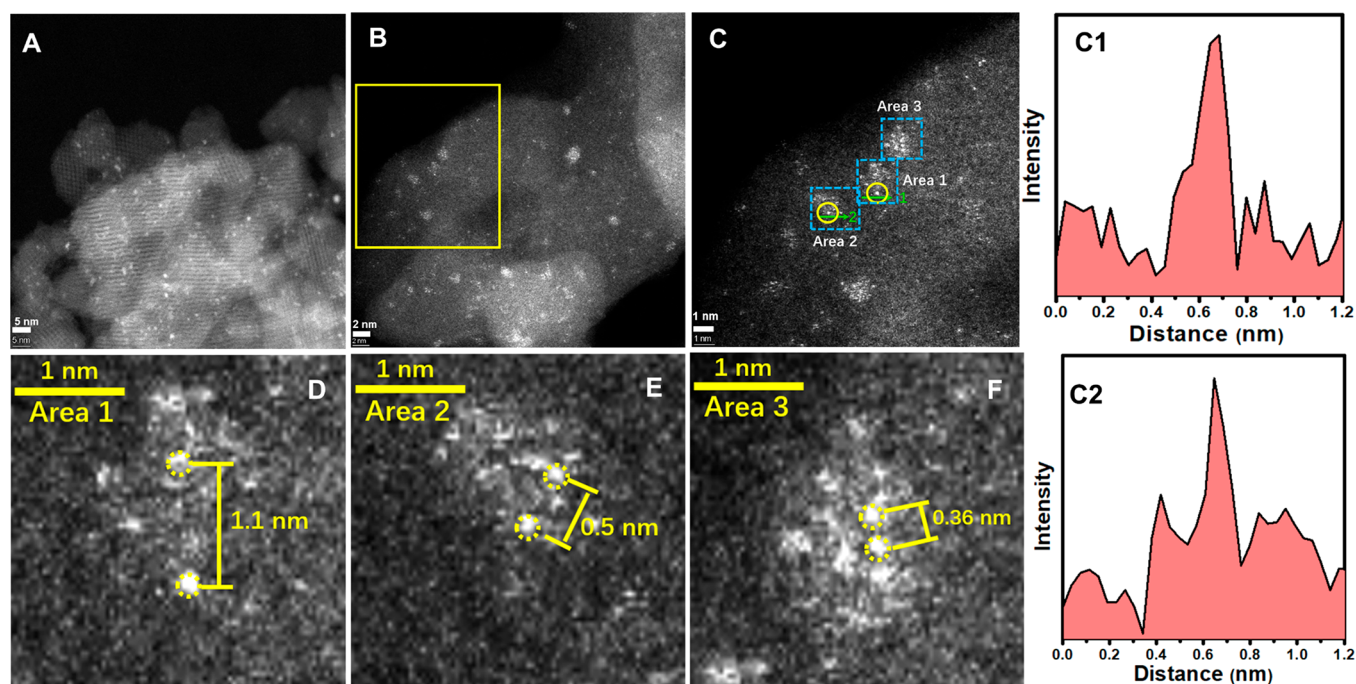


Figure 3. (A and B) HAADF-STEM images of as-prepared 0.04Pt0.36Zn-DeAlBEA. Panel C is an enlargement of the region in the yellow square in panel B; the yellow circles show the position of Pt atoms; C1 and C2 are intensity profiles along the green arrows in C. Panels D–F are enlarged images of the dotted blue areas (1–3) in panel C, in which the yellow dotted circles are drawn around individual Pt atoms.

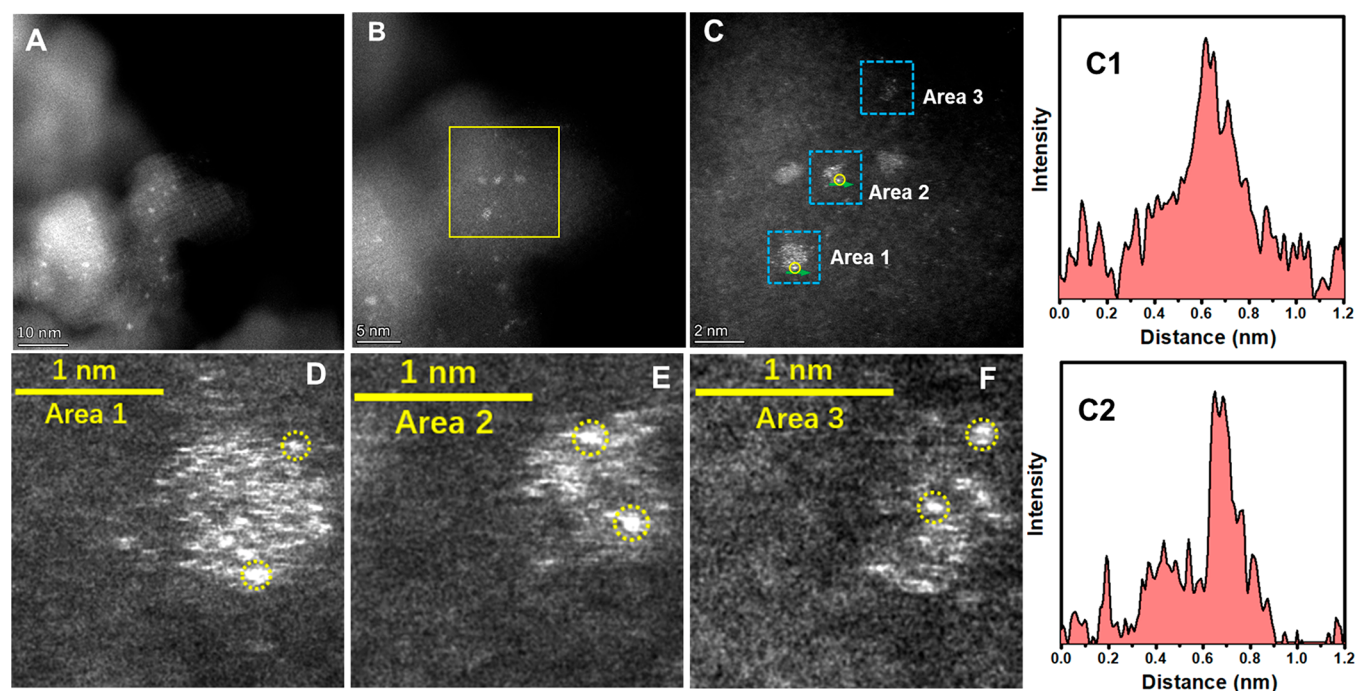


Figure 4. (A and B) HAADF-STEM images of 0.04Pt0.36Zn-DeAlBEA after He pretreatment at 823 K. Panel C is an enlargement image of the yellow square in panel B, with the yellow circles showing the position of Pt atoms; C1 and C2 are intensity profiles along the green arrows in panel C. Panels D–F are enlargements of the dotted blue areas (1–3) in panel C, in which the dotted yellow circles are drawn around individual Pt atoms.

Cs-corrected, high-angle annular dark-field scanning transmission electron micrographs (HAADF-STEM) of Zn-DeAlBEA with Zn/Al ratios of 0.12–0.36 are presented in Figure S4A–C in the Supporting Information. Individual Zn atoms could not be distinguished in the images of 0.12Zn-DeAlBEA (Figure S4A), even with 2 nm resolution, and only the lattice image of the BEA zeolite is evident, indicating the extremely

high dispersion of the introduced Zn atoms. As the Zn/Al ratio increased to 0.24 (Figure S4B) and then 0.36 (Figure S4C), very small Zn clusters (1–2 nm in diameter) appeared; smaller Zn clusters were challenging to image because of the low atomic number of Zn and the weak contrast with the atoms of the zeolite support.

Further detailed information about the $\equiv\text{SiOZn-OH}$ species was obtained from X-ray absorption spectra recorded at the Zn K-edge for 0.36Zn-DeAlBEA after a pretreatment in He at 823 K. The Zn K-edge EXAFS data show that the Zn nests were characterized by a Zn–O coordination number of 2.0 ± 1.0 at a bonding distance of $1.88 \pm 0.08 \text{ \AA}$ and a Zn–(O)–Si coordination number of 0.8 ± 0.6 , consistent with the presence of Zn in a mixture of species within the silanol nests and with the UV–vis and STEM results. Because the data also show a Zn–Zn coordination number of about 1 at a distance of 2.66 \AA (Table 1 and Figure 2), we infer that some of the Zn atoms were located in close proximity to one another within the nests.

In summary, the IR, UV–vis, and NMR spectra demonstrate that Zn Lewis acid sites introduced into the silanol nests of DeAlBEA are stabilized by M–O–Si bonds. The STEM images demonstrate the presence of $\equiv\text{SiOZn-OH}$ nests, and the UV–vis spectra, STEM images, and XAS data suggest that these groups interact weakly with each other. As discussed in the next section, the 0.36Zn-DeAlBEA was chosen as the support for Pt atoms.

Dispersion of Pt in $\equiv\text{SiOZn-OH}$ Nests. Pt was added to Zn-DeAlBEA as described in Experimental Methods. HAADF-STEM images of as-prepared 0.04Pt-0.36Zn-DeAlBEA at various resolutions are presented in Figure 3A–F. The white spots evident in panels A and B of Figure 3, taken with resolutions of 5 and 2 nm, respectively, might at first be taken as evidence of nanoparticles. However, when the resolution is increased to 1 nm (Figure 3C), it is clear that these spots comprise isolated Pt atoms. An enlargement of areas 1–3 in Figure 3C is shown in Figure 3D–F; panels C1 and C2 in Figure 3 show line scans of the signal intensity for areas 1 and 2. The bright spots in Figure 3C1,C2 have diameters of $\sim 0.2 \text{ nm}$, consistent with their assignment to individual Pt atoms. Figure 3D–F shows that the Pt atoms are spaced $3.6\text{--}11 \text{ \AA}$ apart. We emphasize that these distances are markedly longer than bonding distances and specifically longer than those in PtZn alloy nanoparticles, for which distances of $2.69\text{--}2.86 \text{ \AA}$ have been reported, consistent with the value of 2.84 \AA for bulk crystalline PtZn alloy.^{8,10,14} The dispersion of Pt in as-prepared 0.04Pt-0.36Zn-DeAlBEA as isolated atoms is a consequence of the novel synthesis method, whereby Pt is introduced into nests of $\equiv\text{SiOZn-OH}$ groups grafted into DeAlBEA. In the absence of such groups in the support, however, the introduction of Pt produces Pt nanoparticles that are $5\text{--}20 \text{ nm}$ in diameter and clearly evident in the HAADF-STEM image shown in Figure S4D in the Supporting Information.

XRD and BET measurements (Table S1 in the Supporting Information) confirm retention of the BEA zeolite framework and the surface area of the support after the introduction of Pt. ^1H NMR spectra show that the addition of Pt to the material leads to consumption of $\equiv\text{SiOZn-OH}$ species, bringing about a lower intensity of the peak at about 2.4 ppm (Figure 11).^{43,47} $^1\text{H}\text{--}^{29}\text{Si}$ CP NMR spectra show an unchanged SiO_4 resonance peak centered at an isotropic chemical shift of -111 ppm (the same position observed for DeAlBEA and 0.36Zn-DeAlBEA, Figure S3 in the Supporting Information), with a peak line width of 4.4 ppm . The two $\equiv\text{Si-OH}$ peaks are centered at an isotropic shift of -103 ppm with a line width of 4.6 ppm , along with a broad peak at -99.6 ppm having a line width of 6.1 ppm . The signal ascribed to $\equiv\text{SiOZn-OH}$ shows a significant shift to -90.0 ppm and a line width of 6.4 ppm . Previous work has shown that the isotropic chemical shift of ^{29}Si in silicate materials is highly sensitive to the Si–O–X bond angle (where X

= Si or Zn) and distance.^{44–46} The addition of Pt to the 0.36Zn-DeAlBEA causes a wider distribution of Si–O–X bond angles, which is reflected by a broadening and change in the ^{29}Si isotropic chemical shift of the $\equiv\text{Si-OH}$ peak at -99.6 ppm and the presence of $\equiv\text{SiOZn-OH}$ species at -90.0 ppm .

Additional information about the Zn and Pt environments in as-prepared 0.04Pt-0.36Zn-DeAlBEA was obtained from X-ray absorption spectra recorded at the Zn K and Pt L_{III} edges. The XANES spectra at these edges indicate that the formal oxidation state of Zn continued to be 2+ and that of Pt 4+ after incorporation of Pt. Further, the Zn K-edge EXAFS data show that the $\equiv\text{SiOZn-OH}$ nests continued to have a Zn–Zn CN of about 1 (Figures 2 and 6, Table 1; Figures S24 and S25 in the Supporting Information), similar to that of the $\equiv\text{SiOZn-OH}$ nests prior to incorporation of Pt. Modeling of the Pt L_{III} -edge EXAFS data is consistent with the presence of single, isolated Pt atoms.

Fitting of the Pt L_{III} -edge EXAFS data also indicates that each Pt atom, on average, is coordinated to a number of Zn atoms, with the number being in the range of about 4–6 (Figure 6B and Table S1A and Figure S15 in the Supporting Information). There is uncertainty associated with this coordination number. We thus fitted the Pt L_{III} -edge EXAFS data using several models, with this coordination number being a variable and, alternatively, with the value being constrained to be 4, 5, or 6 (Table S1A in the Supporting Information). With the Pt–Zn CN being a variable in the fitting, we found the value giving the best fit according to the R-factor was 6 (Table S1A in the Supporting Information). However, the $\Delta\sigma^2$ parameter, accounting for Debye–Waller-like distortion, is large for a single scattering path at a bonding distance. This large $\Delta\sigma^2$ value implies variations in Zn coordination environments (a mixture). This result can be attributed to the presence of multiple scattering paths at similar distances that cannot be resolved in a single structural model representing the sample. (We emphasize that interference patterns in these similar scattering paths lead to variations in the CN and $\Delta\sigma^2$ values, because these two parameters are highly correlated in the EXAFS fitting.) Thus, proceeding with the values constrained as stated above, we found satisfactory fits when the CN was fixed at 4, 5, or 6 (Table S1A in the Supporting Information). Significantly, the fitted $\Delta\sigma^2$ values decreased as the constrained CN value decreased from 6 to 4 (Table S1A in the Supporting Information) along with an increase in the R-factor, a metric determining the goodness of fit. Thus, we conclude that the data are consistent with the presence of a mixture of species in the nests, represented as $(\equiv\text{Si-O-Zn})_{4-6}\text{Pt}$.

As discussed below, we found that for 0.04Pt-0.36Zn-DeAlBEA to exhibit stable activity for PDH, it was necessary to pretreat the as-prepared material in He at 823 K for 0.5 h. We therefore characterized this material following this pretreatment (Figure 6) in order to establish what changes occurred in both the Zn and Pt environments.

As shown in Figures S6A and S7 in the Supporting Information, the white line of the as-synthesized Pt L_{III} -edge XANES spectrum decreased in intensity when the sample was heated to 823 K in flowing He—to an intensity essentially matching that of metallic Pt. These results also show three isosbestic points in the spectra (Figure 5) that are clearly evident in the data characterizing changes occurring during the pretreatment, demonstrating that stoichiometrically simple changes took place in the ligand environment of Pt during the treatment.^{48–50} This observation suggests that a smooth

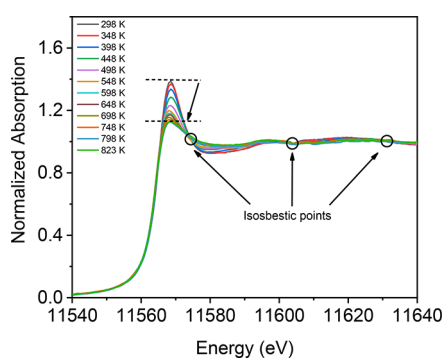


Figure 5. Isosbestic points of Pt L_{III} XANES spectra during treatment. Pt L_{III} XANES spectra of 0.04Pt-0.36Zn-DeAlBEA recorded during treatment in flowing He as temperature was ramped from 298 to 823 K.

transformation from the initial to the final set of structures occurred during the pretreatment. This behavior is not what would be expected if the initial isolated Pt atoms had been transformed into Pt and/or PtZn alloy nanoparticles with a range of compositions (and sizes). HAADF-STEM images (Figure 4) of 0.04Pt-0.36Zn-DeAlBEA after the pretreatment are very similar to those of the as-synthesized sample, further indicating that the Pt atoms were very well isolated before and after pretreatment.

Zn K-edge XANES data for 0.04Pt-0.36Zn-DeAlBEA show that heating shifted the absorption edge to lower energy, from that of Zn^{2+} initially to that of Zn with an average oxidation state of +1 (Figures S9–S11 in the Supporting Information), indicating a mixture of species suggested to be Zn^0 and Zn^{2+} . Thus, both the Pt and Zn were reduced upon heating of the sample in flowing He, implying some form of autoreduction.

Although we attempted to identify the gas-phase products of this process using online mass spectrometry, the sensitivity of the instrument was not sufficient to establish what products had formed.

Heating to 823 K in flowing He led to a marked change in the Pt L_{III} -edge EXAFS pattern of 0.04Pt-0.36Zn-DeAlBEA. Modeling of these data revealed the presence of only a single Pt–Zn scattering path, with a Pt–Zn distance of $2.54 \pm 0.10 \text{ \AA}$, and, again, a coordination number between 4 and 6 (Figures 6C and S17 and Tables 2 and S1A).^{10,14} We emphasize that, as for the as-prepared sample, there is uncertainty in the coordination number. Thus, the data, shown in Table 2 and Figures S18 and S19 in the Supporting Information, with additional fitting done with constrained values of the Pt–Zn coordination number as shown in Table S1A in the Supporting Information, do not determine a single structure and are instead consistent with a range of structures, leading to the conclusion that the average number of Zn atoms coordinated to Pt is best described as being in the range of 4–6. The data could not be fitted with a Pt–Pt scattering path that would have indicated the presence of Pt clusters (Figure S20 in the Supporting Information).

The data do not determine the fraction of the $\equiv SiOZn-OH$ nests containing Pt; however, the HAADF-STEM images (Figure 3C) suggest that it was less than 1. An important result is that these findings are inconsistent with the formation of PtZn clusters or PtZn alloy nanoparticles. It has been reported that in PtZn clusters containing roughly three Pt atoms each,⁸ the Pt–Pt CN is ca. 2.1, whereas, to repeat, for PtZn alloy nanoparticles, the Pt–Pt CN is in the range of 1.6–3.6.^{10,14} In sharp contrast, our results show that for 0.04Pt-0.36Zn-DeAlBEA pretreated in He at 823 K the Pt–Pt CN is indistinguishable from 0 (in agreement with the observations mentioned above for the as-

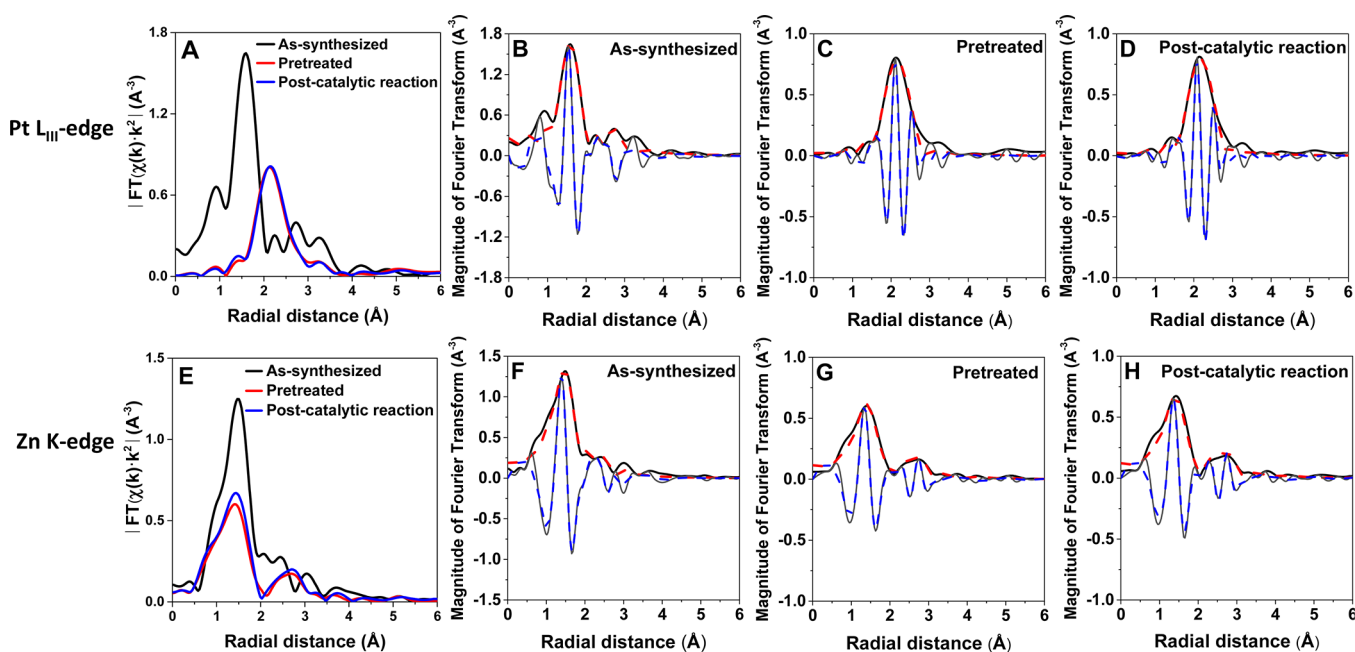


Figure 6. XAS results characterizing 0.04Pt-0.36Zn-DeAlBEA. (A) Pt L_{III} -edge EXAFS data (magnitude of the Fourier transform (FT) (k^2 -weighted)), (B–D) Pt L_{III} -edge EXAFS data and results of EXAFS modeling, (E) Zn K-edge EXAFS data (magnitude of the FT (k^2 -weighted)), and (F–H) Zn K-edge EXAFS data and results of EXAFS modeling for 0.04Pt-0.36Zn-DeAlBEA after various treatments: (A and E) as-synthesized 0.04Pt-0.36Zn-DeAlBEA (pressed into a pellet) at 298 K in air (black), 0.04Pt-0.36Zn-DeAlBEA exposed to flowing He at 823 K for 30 min (red), and 0.04Pt-0.36Zn-DeAlBEA after reaction in flowing C_3H_8/He mixture (C_3H_8/He molar ratio = 1:3 at 723 K for 30 min (blue)). (B–D and F–H) imaginary part (solid grey line) and magnitude of the FT (k^2 -weighted) of data (solid black line), and the calculated contribution (dashed red line). The range in k was 3.0 – 10.0 \AA^{-1} , and the fitted range in radial distance was 1.0 – 3.3 \AA .

Table 2. Summary of Fit Parameters Representing EXAFS Data at Pt L_{III} Edge Characterizing 0.04Pt-0.36Zn-DeAlBEA as Synthesized and after Treatments under Various Conditions^a

sample	scattering path	N^b	R (Å)	$\Delta\sigma^2 \times 10^3$ (Å ²)	ΔE_0 (eV)	R-factor	reduced χ^2
as-synthesized 0.04Pt-0.36Zn-DeAlBEA, model 1	Pt–O _s	5.6 ± 1.0	1.99 ± 0.04	4 ± 2	10.3 ± 2.0	0.02	431
as-synthesized 0.04Pt-0.36Zn-DeAlBEA, model 2	Pt–O _s	5.4 ± 0.6	1.99 ± 0.04	3 ± 1	10.0 ± 1.1	0.01	142
	Pt–(O)–Si	2.1 ± 0.8	3.31 ± 0.07	3 ± 3	6.4 ± 3.1		
as-synthesized 0.04Pt-0.36Zn-DeAlBEA, model 3	Pt–O _s	5.0 ± 1.6	2.00 ± 0.05	3 ± 4	10.8 ± 6.4	0.05	2233
	Pt–(O)–Pt	1.0 ± 1.9	3.17 ± 0.10	8 ± 10	−9.6 ± 42.0		
pretreated 0.04Pt-0.36Zn-DeAlBEA, model 1	Pt–Zn	6.1 ± 0.4	2.54 ± 0.10	9 ± 1	1.8 ± 0.5	0.02	215
pretreated 0.04Pt-0.36Zn-DeAlBEA, model 2	Pt–Zn	5 ^c	2.55 ± 0.09	8 ± 2	1.8 ± 0.5	0.02	627
pretreated 0.04Pt-0.36Zn-DeAlBEA, model 3	Pt–Zn	4 ^c	2.55 ± 0.09	6 ± 1	1.8 ± 0.5	0.02	981
postcatalytic reaction 0.04Pt-0.36Zn-DeAlBEA	Pt–Zn	6.0 ± 0.2	2.55 ± 0.09	9 ± 1	1.7 ± 0.8	0.02	193

^aThe range in k was 3.0–10.0 Å^{−1}, and the fit range in distance r was 1.0–3.3 Å. For a more detailed fitting, with constrained values of the Pt–Zn coordination number, see Table S1A in the Supporting Information. ^bNotation: N , coordination number; R , scattering path length between the absorber and the backscatterer atom; $\Delta\sigma^2$, mean square relative displacement; ΔE_0 , inner potential correction. O_s denotes single-scattering Pt–O_s, Zn single-scattering Pt–Zn, and Pt single-scattering Pt–Pt. The R -factor is a measure of how closely the fit resembles that data. The reduced χ^2 is a statistical fitting metric normalized by the degrees of freedom. ^cThese values were fixed in the fitting. Model 1 of the pretreated sample indicates a better reduced χ^2 value than models 2 and 3.

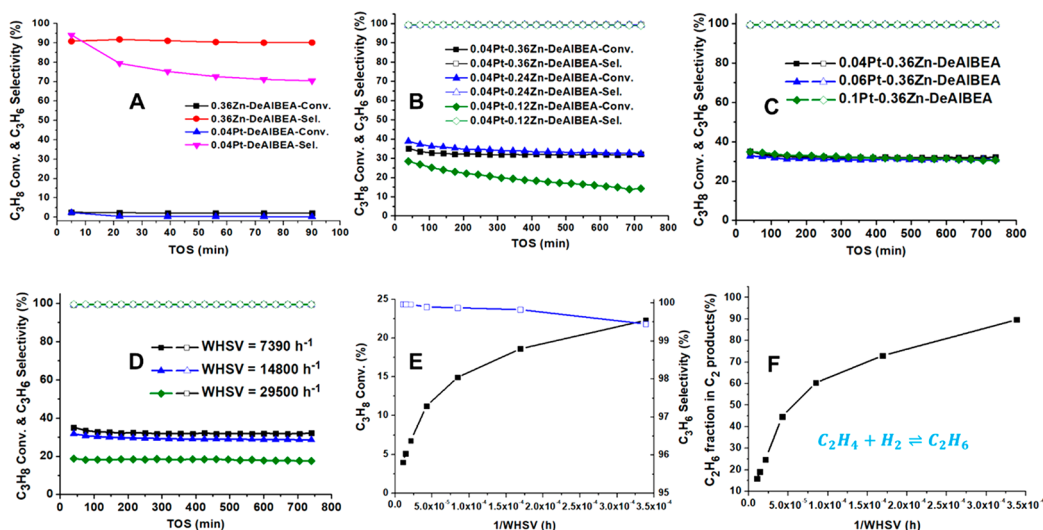
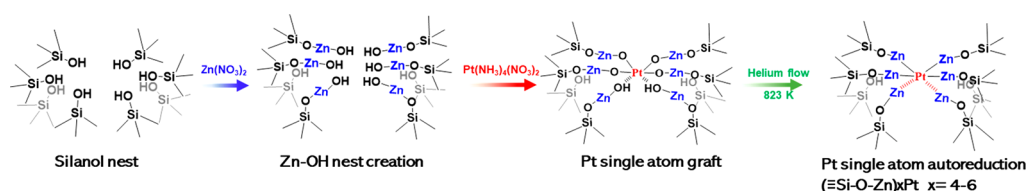
Scheme 1. Simplified Illustration of the Formation of a Pt Single-Atom Catalyst

Figure 7. Catalyst performance data. (A) Propane conversion and propene selectivity for PDH catalyzed by 0.04Pt-DeAlBEA and 0.36Zn-DeAlBEA; (B) effects of Zn loading of 0.04Pt- x Zn-DeAlBEA on the propane conversion and propene selectivity; (C) effects of Pt loading of x Pt-0.36Zn-DeAlBEA on the propane conversion and propene selectivity; (D) effects of WHSV on propane conversion and propene selectivity catalyzed by 0.04Pt-0.36Zn-DeAlBEA at 823 K; (E and F) effects of 1/WHSV on propane conversion and propene selectivity and the fraction of ethane in C₂ products for PDH reaction catalyzed by 0.04Pt-0.36Zn-DeAlBEA at 773 K. Reaction conditions (A–C): 0.02 g of catalyst for 0.04Pt- x Zn-DeAlBEA ($x = 0.12, 0.24, 0.36$), 0.04Pt-DeAlBEA, and 0.36Zn-DeAlBEA; 0.011 and 0.007 g of catalyst for 0.06Pt-0.36Zn-DeAlBEA and 0.1Pt-0.36Zn-DeAlBEA, respectively, each mixed with 0.04 g of SiO₂; atmospheric pressure, C₃H₈/He = 10/30 mL(NTP) min^{−1}, $P_{C_3H_8} = 25.3$ kPa. Reaction conditions (E–F): 0.01 g of catalyst, $P_{C_3H_8} = 20.3$ kPa. Note: WHSV is defined as the ratio of the mass flow rate of propane to the mass of Pt in the catalyst.

synthesized sample), indicating the extremely high dispersion of the Pt and verifying the STEM images shown in Figure 4D–F, which—we reemphasize—provide the best basis for quantifying the Pt dispersion.

The EXAFS data taken after the use of pretreated 0.04Pt-0.36Zn-DeAlBEA for PDH for 1 h gave the same parameters (within error) as those for the He-pretreated catalyst, indicating

that the Pt–Zn structure is stable under reaction conditions (Figure 6D, Table 2, and Figure S21 in the Supporting Information). HAADF-STEM images (Figure S8) also show that after 3 h of reaction at 823 K with a weight hourly space velocity (WHSV) of 7390 g_{C₃H₈}/g_{Pt}/h (which we, by convention, refer to below in dimensions of h^{−1}, *vide infra*), the Pt atoms remained very highly dispersed.

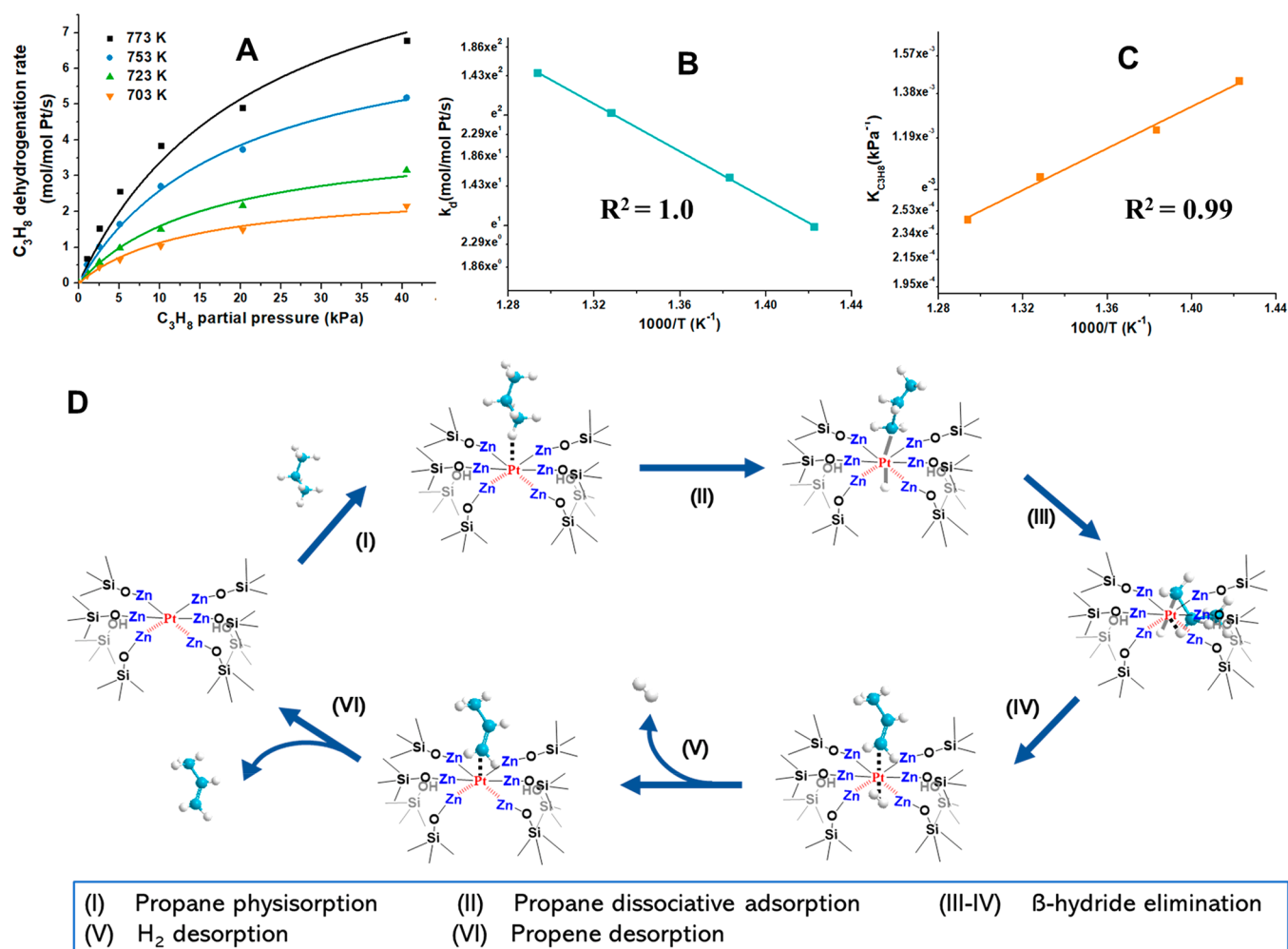


Figure 8. (A) Rate of propene formation catalyzed by 0.04Pt-0.36Zn-DeAlBEA as a function of propane partial pressure at various temperatures. The solid lines for C₃H₆ formation represent a fit of data to eq S9. (B) Arrhenius plot characterizing propane dehydrogenation rate constants and (C) van't Hoff plot characterizing propane adsorption equilibrium constant determined from fit of data to eq S9. (D) Proposed reaction mechanism for PDH on isolated Pt atoms.

The Zn K-edge EXAFS data also provide evidence for the formation of the catalytically active species. Heating in He reduced the average Zn–O CN from 4 in the as-prepared sample to 2, with a Zn–O distance of 1.90 ± 0.06 Å. The best-fit model indicates the presence of the aforementioned Zn–Zn contribution similar to that of metallic Zn, at 2.70 ± 0.04 Å (Figure 6G, Table 1, and Figure S26 in the Supporting Information), but the data are not sufficient to fit the expected Zn–Pt scattering path (see the Supporting Information for details). These results, combined with the Pt L_{III} edge data, point to small zinc nests containing isolated Pt atoms. Consistent with the Pt XAS data, *in situ* Zn XAS data show almost no change during catalysis (Figure 6E, Table 1, and Figures S9 and S30 in the Supporting Information).

Scheme 1 summarizes the chemistry of formation and activation of Pt sites deduced from an examination of all of the characterization data presented above. The first step involves dealumination of zeolite H-BEA and creation of silanol nests (consisting of four $\equiv\text{Si}-\text{OH}$ groups per Al atom removed). Introduction of Zn creates $\equiv\text{SiOZn}-\text{OH}$ groups. If the silanol nests are created by removal of two proximate Al atoms in 4-, 5-, 6-, or 12-membered rings, then a nest consisting of up to eight $\equiv\text{SiOZn}-\text{OH}$ groups can be created.^{52–54} The existence of

proximate Al sites is reported to be common for BEA zeolite, and for BEA zeolite with a Si/Al of 14, their presence was verified by Co²⁺ ion exchange experiments showing that approximately half of the Al sites are in pairs.⁵⁴ More recently, Tabor et al. reported that both Al pair and “close unpaired Al” atoms are common for BEA zeolite and that the fraction of Al in NNN and NNNN pairs can vary from 40 to 65% in BEA for Si/Al < 18.⁵³ Pt grafted into such a $\equiv\text{SiOZn}-\text{OH}$ nest interacts on average with four to six O atoms of the ZnOH groups. When the as-prepared structure is heated in He, autoreduction occurs to produce Pt atoms interacting with four to six nearest-neighbor Zn atoms but no O atoms. Taken together, the evidence from multiple analytical methods leads to the deduction that Pt is atomically dispersed and bound in the form $(\equiv\text{Si}-\text{O}-\text{Zn})_{4-6}\text{Pt}$ complexes. Evidence suggesting the plausibility of such structures is provided by a comparison with structure data characterizing a pure compound, $[\text{Pd}(\text{ZnCp}^*)_4(\text{CNTbu})_2]$.⁵¹ The XRD-determined Pd–Zn lengths reported for this complex range from 2.43 to 2.48 Å, and the Zn–Zn distances are all 2.6 Å. The Pd–Zn distance is only slightly shorter than that characterizing Pt–Zn, 2.54–2.55 Å, determined for our catalyst by EXAFS spectroscopy, and the Zn–Zn distance matches that determined for our catalyst by EXAFS spectroscopy, 2.7 Å (Table 1).

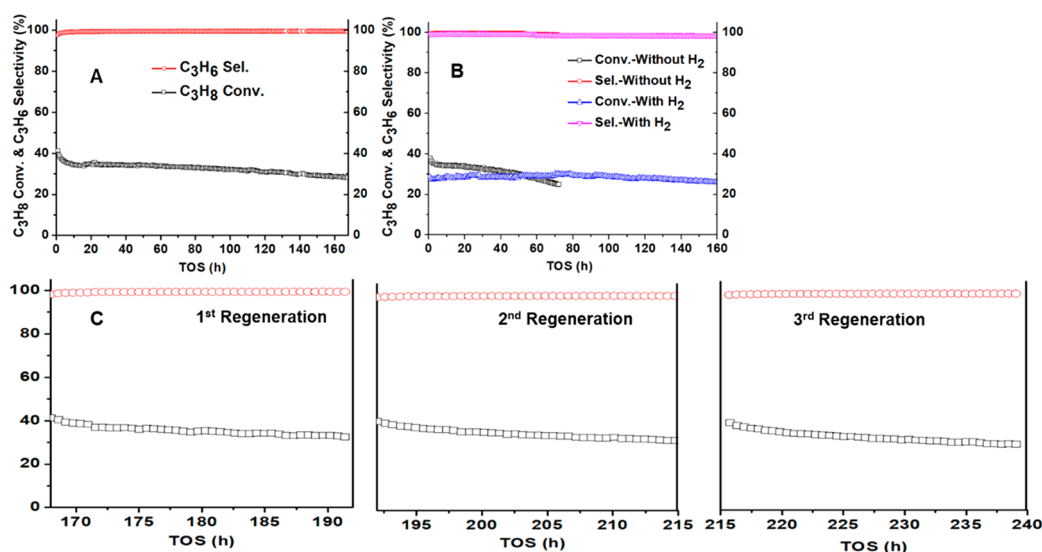


Figure 9. Long-term stability test. (A) Long-term stability test for PDH catalyzed by 0.04Pt-0.36Zn-DeAlBEA without co-fed H_2 ($P_{C_3H_8} = 25.3$ kPa, WHSV = 1477 h^{-1} , 823 K). (B) Long-term stability test for PDH catalyzed by 0.04Pt-0.36Zn-DeAlBEA with and without H_2 in the feed ($P_{C_3H_8} = 25.3$ kPa, $P_{H_2} = 7.6$ kPa, WHSV = 7390 h^{-1} , 823 K). (C) PDH catalyzed by regenerated 0.04Pt-0.36Zn-DeAlBEA [after 160 h PDH test, (A)] ($P_{C_3H_8} = 25.3$ kPa, WHSV = 1477 h^{-1} , 823 K).

Catalyst Performance. The PDH activity and selectivity of 0.04Pt-DeAlBEA, 0.36Zn-DeAlBEA, and 0.04Pt-0.36Zn-DeAlBEA are presented in Figure 7 for one set of reaction conditions. 0.04Pt-DeAlBEA and 0.36Zn-DeAlBEA exhibited comparable and very low propane conversions of 2.4% and 2.5%, respectively, and propene selectivities of 94% and 91%, respectively. However, the propene selectivity of 0.36Zn-DeAlBEA is more stable than that of 0.04Pt-DeAlBEA, which steadily declined with time on stream (TOS). By contrast, 0.04Pt-0.36Zn-DeAlBEA pretreated in He exhibited both high activity (propane conversion $\sim 32\%$), high propene selectivity ($>99\%$), and excellent stability over 12 h of continuous operation (Figure 7B). Thermal gravimetric (TG) analysis showed that ~ 2.7 wt % coke accumulated after 12 h of reaction ($P_{C_3H_8} = 25.3$ kPa, WHSV = 7390 h^{-1} , 823 K) (Figure S31A in the Supporting Information), corresponding to about 1.3×10^{-4} $g_{\text{coke}}/g_{C_3H_8}$ on average. We also note that after 12 h of reaction, ICP analysis showed that the catalyst Zn content decreased from ~ 2.4 to ~ 2.0 wt %, with no detectable loss of Pt, so that the Zn:Pt ratio was 8.

The influence of Zn loading on performance was evaluated for catalysts with a constant Pt:Al atomic ratio of 0.04. (Al concentration in the original H-BEA is used as a proxy for the concentration of silanol nests in DeAlBEA.) As the Zn:Al atomic ratio increased from 0.12 to 0.36, the propene selectivity remained $>99\%$ for all catalysts (Figure 7B). However, the activity increased somewhat as the Zn/Al ratio increased from 0.12 to 0.24, becoming almost constant for Zn/Al > 0.24 . Increasing the Zn/Al ratio (at a constant Pt/Al ratio) improved catalyst stability, as more neighboring Zn sites were available to isolate and anchor Pt atoms. The influence of Pt loading was investigated separately with 0.36Zn-DeAlBEA (chosen as the near-optimal Zn:Al ratio for stabilizing Pt atoms) (Figure 7C). When the Pt:Al ratio was increased from 0.04 to 0.06 and 0.10 (at a constant Zn:Al ratio of 0.36), the mass of catalyst used for each test was decreased correspondingly to keep the space velocity (now defined as the molar flow rate of propane per Pt

atom) unchanged. Virtually the same activity, selectivity, and stability were observed for reactions carried out for Pt:Al ratios of 0.04 and 0.06. For 0.1Pt-0.36Zn-DeAlBEA, for which Zn:Pt = 3.6, the activity and selectivity were similar to that observed for higher Zn:Pt ratios, but the catalyst was less stable (the first-order deactivation rate constant k_{deac} increased from 0.004 to 0.014 h^{-1} , Figure S31B in the Supporting Information), indicating that the Zn:Pt ratio should be kept at values > 4 in order to maintain catalyst stability.

The reaction kinetics and time-on-stream stability of 0.04Pt-0.36Zn-DeAlBEA were examined in detail. When the WHSV increased from 7390 to 29500 h^{-1} at 823 K, the conversion decreased from 32 to 18.3% (Figure 7D); the propene selectivity remained $>99\%$; no deactivation occurred during 12 h of reaction. For reaction at WHSV = 29500 h^{-1} , the propene turnover frequency (TOF) was $\sim 6.8\text{ mol C}_3\text{H}_6\text{ (mol Pt)}^{-1}\text{ s}^{-1}$ (corresponding to a productivity of $\sim 125\text{ mol C}_3\text{H}_6\text{ (g Pt)}^{-1}\text{ h}^{-1}$).

A more detailed investigation of the influence of WHSV was performed at 773 K. Figure 7E shows the effects of $1/\text{WHSV}$ on propane conversion to propene and the fraction of ethane in C_2 products for the reaction of propane catalyzed by 0.04Pt-0.36Zn-DeAlBEA at 773 K. As the space time ($1/\text{WHSV}$), which is proportional to the residence time, increased, the conversion of propane to propene increased but then approached the equilibrium value at 773 K (28.9% at 773 K and an initial propane partial pressure 20.3 kPa). The blue curves show that, coincidentally, the propene selectivity slightly decreased from near 100% to about 99.5% because of the enhanced cracking of propane at higher space times. Moreover, as is shown in Figure 7F, the proportion of ethane formed by hydrogenation of ethene, produced from cracking a small fraction of the propane to methane and ethene, underwent hydrogenation to ethane as $1/\text{WHSV}$ increased.

A mechanism for PDH on isolated Pt atoms is proposed in Figure 8D. This scheme is based on our previous density functional theory (DFT) studies of PDH on Pt_4 clusters⁵⁵ and related studies of PtZn¹⁰ and PtGa⁹ intermetallic alloy catalysts.

Propane adsorption is followed directly by the hydrogen abstraction from a methyl group, leading to a propyl group and an H atom bonded to the Pt atom. The second hydrogen abstraction also takes place on the Pt atom, followed by desorption of propene and hydrogen. Desorption of propene completes the catalytic cycle. Physisorption of propane is taken to be quasi-equilibrated and the dissociation of the first C–H bond to be rate-limiting. With these assumptions, the dependence of the rate of PDH on propane partial pressure is given by eq 1 (derived in section S4 of the Supporting Information, Derivation of Rate Expression for Propane Dehydrogenation Catalyzed by Isolated Pt Single Sites). In eq 1, the symbols $r_{\text{C}_3\text{H}_6}$, k_{d1} , $K_{\text{C}_3\text{H}_8}$, and $P_{\text{C}_3\text{H}_8}$ represent propene formation rate, rate constant for the first C–H bond cleavage as rate-limiting step, adsorption equilibrium constant of propane, and propane partial pressure, respectively.

$$r_{\text{C}_3\text{H}_6} = \frac{k_{\text{d1}}K_{\text{C}_3\text{H}_8}P_{\text{C}_3\text{H}_8}}{1 + K_{\text{C}_3\text{H}_8}P_{\text{C}_3\text{H}_8}} \quad (1)$$

The kinetics of PDH were measured at high space velocities (low conversions) to minimize the influence of propene hydrogenation (Figure 8A–C). Figure 8A demonstrates that eq 1 properly describes the reaction kinetics. The activation energy determined from an Arrhenius plot for the dehydrogenation rate coefficient (k_{d1}) is 90 kJ/mol. This value is lower than the activation energy for the first C–H cleavage reported for Pt single atoms in PtGa–Pb/SiO₂ catalyst (ca. 111.7 kJ/mol).⁹ The enthalpy of adsorption for propane on Pt single sites, determined from a van't Hoff plot for the adsorption equilibrium constants ($K_{\text{C}_3\text{H}_8}$), is 29.3 kJ/mol, close to that for Pt and Pt₁–ZnO (27 kJ/mol)⁵⁶ and lower than that for Pt on a 4 × 2 Pt(111) surface (34 kJ/mol).⁵⁷

To determine the long-term stability of the atomically dispersed Pt catalyst, a 160 h stability test was done with 0.04Pt–0.36Zn–DeAlBEA (Figure 9A). Only 10% of the initial steady-state activity was lost over this period—with no hydrogen added to the feed. Three consecutive regenerations and subsequent 24 h PDH tests were performed after the long-term stability test (Figure 9C), and the data show that the fresh activity can be fully reclaimed after each experiment, demonstrating the excellent stability and regenerability of the catalyst. Another long-term stability test was performed at a much higher WHSV (7390 h^{−1}) (Figure 9B), with 7.6 kPa H₂ co-fed with 25.3 kPa propane and other conditions kept the same; the data show enhanced catalyst stability—with almost no deactivation after 160 h on stream. The ICP test showed that the detected Zn content after 160 h of continuous PDH reaction was about 1.2 wt %, which is similar to the value observed after 32 h of continuous PDH reaction, indicating that the Zn loss essentially stopped at around this value. No Pt loss was detected after 160 h of PDH reaction. The final Zn/Pt ratio was about 4.8, which is still in the range of 4–6, consistent with what we proposed for the (≡Si–O–Zn)_{4–6}Pt complex. Thus, we suggest that the zinc that was lost was from structures other than the catalytically active structures.

The observed high PDH stability is attributed to the interaction of Pt atoms with multiple ≡SiOZn–OH groups located within nests in the Zn-functionalized DeAlBEA—consistent with the aforementioned results showing that, upon heating in He, Pt–Zn bonds form via autoreduction, leading to the appearance of the (≡Si–O–Zn)_{4–6}Pt complexes detected

by EXAFS spectroscopy and STEM. The formation of strong Pt–Zn bonds is supported by calculations showing that the bonding of Pt to Zn is stronger than that to Pt.¹⁰ The metal–metal bond energy is calculated to be $E_{\text{Pt–Pt}}$ (−0.46 eV) > $E_{\text{Pt–Zn}}$ (−0.49 eV), and on the basis of the nearest-neighbor approximation and calculated cohesive energies, the energy change associated with the formation of one Pt–Zn bond from Pt–Pt and Zn–Zn bonds is calculated to be −0.17 eV, indicating that the formation of Pt–Zn bonds is favorable energetically.^{10,58} Furthermore, we note that the XANES data show that the Pt atoms in the (≡Si–O–Zn)_{4–6}Pt complexes are slightly positively charged. As noted earlier, previous studies have shown that this charge is conducive to imparting a high propene selectivity.²¹

The comparison of the performance of our catalyst with those reported in previous studies of PtZn catalysts requires that this be done with data collected at the same temperature and with proper accounting for the initial propane partial pressure and the approach to equilibrium, because PDH is a reversible reaction. As discussed in the Supporting Information, such a comparison can be done by computing the apparent rate coefficient, k_f [mol C₃H₆/(g Pt·h·bar)], for PDH at low propane conversions. This can be done using eq 2. Here R_{net} (mol/(g Pt × h)) is the net rate of reaction; $P_{\text{C}_3}^0$ (bar) is the inlet partial pressure of propane; K_e (bar) is the equilibrium constant for PDH; and X is the propane conversion.

$$k_f = \frac{R_{\text{net}}}{P_{\text{C}_3}^0(1 - X) \left(1 - \frac{1}{K_e} \frac{P_{\text{C}_3}^0 X^2}{(1 - X)} \right)} \quad (2)$$

Table S4 in the Supporting Information provides a comparison of values of k_f determined for 0.04Pt–0.36Zn–DeAlBEA with those characterizing PtZn catalysts reported in the literature, all tested at 823 K. The value of k_f for 0.04Pt–0.36Zn–DeAlBEA is 692 mol C₃H₆/(g Pt·h·bar), which is significantly greater than those reported for catalysts incorporating Pt and Zn, which range from 39 to 389 mol C₃H₆/(g Pt·h·bar). Table S4 also shows that although all of these catalysts exhibit propene selectivities in excess of 96%, our catalyst achieves a selectivity of 99.4%. Moreover, the stability of 0.04Pt–0.36Zn–DeAlBEA, defined by k_{deact} is 0.004 h^{−1}, which is among the lowest values reported (0.072–0.003 h^{−1}).

CONCLUSIONS

The results show that isolated Pt atoms are stabilized in nests of ≡SiOZn–OH groups formed by introducing Zn into silanol nests in dealuminated zeolite BEA. Once treated in He at 823 K, the Pt is autoreduced to a nearly zerovalent state, with Zn in an average oxidation state close to +1. Pt is coordinated to as many as about 6 Zn atoms in the activated catalyst. The resulting (≡Si–O–Zn)_{4–6}Pt complex exhibits a PDH activity higher than that of any reported PtZn alloy or cluster catalyst, with nearly 100% propene selectivity and very high stability. In the presence of a low partial pressure of H₂, the catalyst functions with virtually no activity loss after 160 h on stream. We posit that the technique used to prepare isolated Pt atoms described here can be extended to other noble metals and that such stable atomically dispersed catalysts may find application for reactions beyond PDH.

EXPERIMENTAL METHODS

Catalyst Synthesis. Zn-DeAlBEA and Pt-DeAlBEA zeolites were prepared in a two-step process, consisting of dealumination of zeolite H-Beta and subsequent introduction of Zn and Pt species via aqueous impregnation utilizing Zn(NO₃)₂·6H₂O (Alfa Aesar, 99% metal basis) and (NH₃)₄Pt(NO₃)₂ (Sigma-Aldrich, ≥50% Pt basis) as Zn and Pt precursors, respectively. In a typical process, commercial zeolite H-Beta (provided by BASF) with a Si/Al ratio of 13 (determined by ICP analysis) was suspended in 13 M nitric acid at 373 K by stirring for 20 h to obtain DeAlBEA. The resulting powder was filtered, washed with MQ deionized water until a pH of 6–7 was reached, and then dried at 373 K under vacuum overnight. Afterward, the DeAlBEA was impregnated with an aqueous metal nitrate solution. Specifically, the molar concentrations of Zn²⁺ and Pt²⁺ solutions were about 0.044, 0.087, and 0.13 mol/L for M/Al ratios (mols of metal introduced per mol of Al in zeolite H-Beta prior to dealumination) of 0.12, 0.24, and 0.36, respectively. Generally, 1.4 mL of solution was needed for 0.5 g of DeAlBEA. The resulting slurry was dried at room temperature and then further dried at 353 K under vacuum for 2 h. The powder mixture was then ground for 20 min. Finally, the Zn-containing catalyst was calcined at 823 K for 6 h, and the Pt-containing catalyst was calcined at 623 K for 2 h in static air. The final product is labeled as *x*M-DeAlBEA, where *x* indicates the M/Al ratio (0.36Zn-DeAlBEA means the Zn/Al ratio is 0.36). Nearly all Al in zeolite H-BEA was removed by dealumination to produce silanol nests, each containing four ≡Si–OH groups. Therefore, M/Al represents the average number of metal atoms per silanol nest.

Pt-Zn-DeAlBEA zeolites were prepared using Zn-DeAlBEA as a support with subsequent introduction of Pt species via an aqueous impregnation method using (NH₃)₄Pt(NO₃)₂ as the Pt precursor. The molar concentrations of Pt²⁺ solutions were about 0.00146, 0.0292, and 0.044 mol/L for Pt/Al ratios (mols of Pt introduced per mol of Al in zeolite H-Beta prior to dealumination) of 0.04, 0.06, and 0.1, respectively. Generally, 1.4 mL of solution was needed for 0.5 g of Zn-DeAlBEA. The resulting slurry was dried at room temperature and then further dried at 353 K under vacuum for 2 h. The powder mixture was then ground for 20 min. Finally, the catalyst was calcined at 623 K for 2 h in static air. The final products are designated as *x*Pt-*y*Zn-DeAlBEA.

Characterization Techniques. Cs-corrected high-angle annular dark-field scanning transmission electron microscopy (HAADF-STEM) characterization was performed using a double Cs-corrected microscope (FEI Titan Cubed Themis Z), operated at 300 kV. The microscope was aligned prior to each experiment using a cross-grating standard sample.

Fourier transform infrared (FTIR) spectra were acquired using a Thermo Scientific Nicolet 6700 spectrometer equipped with a liquid-nitrogen-cooled MCT detector. For spectra of the hydroxyl stretching region, a spectrum of the empty cell was used as the background, whereas for spectra of adsorbed pyridine, the spectrum of the sample pellet taken prior to pyridine adsorption was used as the background. For IR spectroscopy characterization, 0.036 g of catalyst was pressed into a 20 mm diameter thin self-supporting wafer and then transferred into a custom-built transmission cell fitted with CaF₂ windows. For IR spectroscopy of adsorbed pyridine, each sample wafer was pretreated in flowing He at 773 K for 1 h and then cooled to 393 K prior to acquisition of spectra; 2 μL of pyridine was injected for each experiment, and then the sample was purged with He for 20 min to remove physically adsorbed pyridine.

Powder X-ray diffraction (PXRD) patterns were recorded on a Rigaku X-ray diffractometer using Cu Kα radiation (λ = 0.15418 nm) at 40 kV and 20 mA. BET surface areas were calculated from nitrogen adsorption isotherms obtained using a Micromeritics Gemini VII 2390 surface area analyzer. The Pt and Zn loadings were determined by elemental analysis performed by Galbraith Laboratories, Inc.

For NMR experiments, each sample was packed in a 4 mm zirconia rotor inside a glovebox under an Ar atmosphere. Once the sample had been packed, the rotors were immediately placed inside a 4 mm Bruker CPMAS probe operated with a ¹H resonance frequency of 500 MHz and spun at a rate of 10 kHz using dry N₂ gas. Quantitative ¹H NMR

data were acquired using the DEPTH pulse sequence with a recycle delay of 2 s and a radio frequency power of 80 kHz. Figure 1G–I shows the ¹H NMR spectra normalized by the maximum intensity of each individual spectrum. The spectra were deconvoluted into individual components with Dmfit software.⁵⁹

¹H–²⁹Si cross-polarization spectra were acquired using a contact pulse of 2000 μs and 80 kHz proton decoupling during ²⁹Si detection, and 1024 scans were acquired. This method uses the dipolar coupling between the ¹H and ²⁹Si spins in the material to transfer the magnetization, and as such it is not quantitative; the resulting intensity will be weighted toward the ²⁹Si species with neighboring proton spins. Figure S3 shows the resulting ²⁹Si spectra for each material normalized to the peak intensity, and the resulting ²⁹Si spectra were deconvoluted into individual components using a Gaussian peak fitting in Dmfit software.

XAS measurements were made at beamline 9-3 at the Stanford Synchrotron Radiation Lightsource (SSRL). Beamline 9-3 is a side-station of a 20 pole, 2 T, wiggler insertion device, with rhodium-coated optics for collimation and harmonic rejection and focusing of the X-ray beam. Photon energy selection was achieved with a double-crystal, liquid-nitrogen-cooled Si(220), Φ = 0, monochromator. Spectra were collected in fluorescence detection mode using a PIPS detector. For Pt L_{III}-edge measurements, platinum foil reference was scanned simultaneously with the sample for energy calibration. For Zn K-edge measurements, a zinc foil reference was scanned simultaneously with the sample for energy calibration. Continuous extended X-ray absorption fine structure (EXAFS) spectra were measured at 298 K from 200 eV below the Pt L_{III}-edge (11564 eV) to *k* = 15.3 Å⁻¹ (*k* is the wavenumber), and at 298 K from 200 eV below the Zn K-edge (9659 eV) to *k* = 15.3 Å⁻¹ in a period of 4 min, with three scans collected and averaged to improve the signal-to-noise ratio under all conditions.

Two separate XAS measurements were made per sample (at the Pt L_{III}-edge and at the Zn K-edge) with the same procedure. EXAFS data characterizing the as-synthesized 0.04Pt-0.36Zn-DeAlBEA were collected at 298 K with the sample pressed into a pellet. For *in situ* treatment of the sample, approximately 40 mg of sample was loaded into an *in situ* XAS cell.⁶⁰ Continuous EXAFS spectra were collected to provide *in situ* XANES data during treatment of the catalyst in flowing He as the temperature was ramped from 300 to 823 K at a rate of 10 K/min followed by a dwell of 30 min at 823 K. The catalyst was then cooled to 298 K to characterize the structure of the treated species by EXAFS spectroscopy. *In situ* XANES data were collected during the temperature ramp with the sample in a flowing mixture of C₃H₈ + He (*P*_{C₃H₈} = 25.3 kPa), followed by a dwell for 30 min at 723 K. EXAFS data were collected at 298 K with the sample in flowing He; these data were intended to characterize local structure around the metal (platinum at the Pt L_{III}-edge and zinc at the Zn K-edge).

Athena and Artemis software, parts of the Demeter package,⁶¹ were used for analysis of the EXAFS data. Preprocessing of data included alignment, edge calibration, deglitching, normalization, background subtraction, and conversion of data into a chi file for data fitting; all this was done with Athena. The energy at the Pt L_{III}-edge was determined by the first inflection point of the absorption edge data characterizing the reference platinum foil, calibrated to the reported energy, 11564.0 eV. The edge energy at the Zn K-edge was determined by calibration of the samples by using a known glitch (at 9867.05 eV).

The scattering paths for the EXAFS analysis were extracted from known structures from the ICSD database: Pt₃Zn (CIF 1522607), PtO₂ (CIF 1008935), and Pt silicide (CIF 2106969) were used to calculate the phase shifts and backscattering amplitudes representing the Pt–Zn, Pt–O, and Pt–Si single-scattering paths, respectively, at the Pt L_{III}-edge. Zn metal (CIF 9008522) and Zn on silica (CIF 1009030) were used to calculate the phase shifts and backscattering amplitudes representing the Zn–Zn, Zn–O, and Zn–Si single-scattering paths, respectively, at the Zn K-edge.

Fitting was carried out considering *k*¹-, *k*²-, and *k*³-weightings. The fitting ranges in both *k* space and *R* space (*R* is the scattering path distance from the absorbing Pt atom at the Pt L_{III}-edge and the Zn atom at Zn K-edge) in analysis of data characterizing the as-synthesized

sample, pretreated sample, and postcatalytic reaction sample were determined by the data quality; the range in k was $(3.0\text{--}10.0) \pm 0.5 \text{ \AA}^{-1}$, and that in r was $(1.0\text{--}3.3) \pm 0.3 \text{ \AA}$. These values were used with the Nyquist theorem⁶² to estimate the justified number of fitting parameters, which was not exceeded in the fitting. Standard procedures were used in the analysis of the XANES spectra.⁶¹

Larch⁶³ was used to perform the continuous Cauchy wavelet transformation⁶⁴ (CCWT) on EXAFS spectra characterizing steady-state conditions of the PtZn/zeolite beta and Zn/zeolite beta samples; k -ranges for the CCWT at the Pt L_{III}-edge and the Zn K-edge were 0.0–10.3 and 0.0–11.7 \AA^{-1} , respectively. The r -range for the CCWT was 0.2–6.0 \AA for each edge.

Measurement of Catalyst Performance. Catalytic tests were conducted using a quartz, packed-bed, downflow reactor (10 mm inner diameter) operated at atmospheric pressure. Quartz wool was placed below the catalyst bed to hold it in place. The reactor temperature was maintained using a tube furnace equipped with a Watlow temperature controller and a K-type thermocouple sensor. Prior to reaction, the catalyst was heated at a rate of 10 K min⁻¹ to 823 K in flowing He (Praxair, 99.999%) at a flow rate of 30 mL min⁻¹ and held for 30 min before the temperature was adjusted to the reaction temperature. No H₂ pretreatment was needed in any of the reaction experiments.

During the activity test at 823 K, a mixture of 10 mL min⁻¹ C₃H₈ (Matheson, Research purity) and 30 mL min⁻¹ He (Praxair, 99.999%) was fed through a bed containing 0.02 g of catalyst with a feeding C₃H₈ partial pressure of 25.3 kPa. The WHSV (Note: WHSV is defined as the ratio of the mass flow rate of propane to the mass of Pt in the catalyst) of propane was approximately 7390 h⁻¹. For experiments carried out with higher values of WHSV (14800 and 29500 h⁻¹), 0.01 g of catalyst was loaded; the C₃H₈ feed partial pressure was kept at 25.3 kPa, and the flow rates of the C₃H₈ and He in the feed mixture were 40 and 80 mL min⁻¹, respectively. To investigate the effect of space time on catalytic performance at 773 K, C₃H₈ at a partial pressure of 20.3 kPa was fed through a bed containing 0.01 g of catalyst, and the total flow rate of the C₃H₈ + He mixture was increased from 10 to 320 mL min⁻¹. For experiments to determine reaction kinetics, the temperature was lowered to 703–773 K, and the total flow rate was increased to 200 mL min⁻¹ to reduce the C₃H₈ conversion to <20% for the lowest partial pressure investigated and <10% for the highest partial pressure investigated.

The catalyst stability tests were performed at 823 K, whereby a mixture of C₃H₈ + He (25:75 vol %) was fed at a rate of 8 mL min⁻¹ to a reactor bed containing 0.02 g of catalyst. The WHSV of propane was approximately 1477 h⁻¹. After the long-term test, the catalyst was regenerated overnight by feeding 20 mL/min of 10% H₂ balanced with He at 723 K. For the catalyst following 24 h of operation in a PDH experiment, 6 h was enough for the second and third regenerations, each carried out by feeding 20 mL/min of 10% H₂ balanced with He at 723 K.

Product streams were analyzed by gas chromatography using an Agilent 6890A GC fitted with a Plot-Q capillary column (30 m × 0.32 mm × 0.25 μm) and a flame ionization detector. The propane conversion and selectivity to propene were calculated from eqs 3 and 4, respectively. The propene productivity is defined as the number of mol of C₃H₆ formed per gram of Pt per hour as presented in eq 5. Here [F_{C₃H₈}] and [F_{C₃H₆}] designate molar flow rates of propane and propene, respectively. N_{Pt} is the mass of Pt in the catalyst.

$$\text{Conv (\%)} = \frac{[F_{\text{C}_3\text{H}_8}]_{\text{inlet}} - [F_{\text{C}_3\text{H}_8}]_{\text{outlet}}}{[F_{\text{C}_3\text{H}_8}]_{\text{inlet}}} \times 100 \quad (3)$$

$$\text{Sel (\%)} = \frac{[F_{\text{C}_3\text{H}_6}]_{\text{outlet}}}{[F_{\text{C}_3\text{H}_8}]_{\text{inlet}} - [F_{\text{C}_3\text{H}_8}]_{\text{outlet}}} \times 100 \quad (4)$$

$$\text{propene productivity} = \frac{[F_{\text{C}_3\text{H}_6}]_{\text{outlet}}}{N_{\text{Pt}}} \quad (5)$$

The deactivation constant, k_{deac} was calculated on the basis of a simple empirical first-order deactivation model^{13,14} used to evaluate the

catalyst stability in eq 6, where Conv_{initial} and Conv_{final} represent the conversions measured at the initial and final stages of a chosen experimental period, respectively, t is time on stream, and the conversion refers to propane.

$$k_{\text{deac}} = \frac{\ln\left(\frac{1 - \text{Conv}_{\text{final}}}{\text{Conv}_{\text{final}}}\right) - \ln\left(\frac{1 - \text{Conv}_{\text{initial}}}{\text{Conv}_{\text{initial}}}\right)}{t} \quad (6)$$

■ ASSOCIATED CONTENT

Supporting Information

The Supporting Information is available free of charge at <https://pubs.acs.org/doi/10.1021/jacs.1c10261>.

Full sets of data (available in the main text or the Supporting Information), including interpretation of NMR spectra; interpretation of XANES Pt L_{III} edge and Zn K edge data; EXAFS data at Pt L_{III} edge and Zn K edge; catalyst characterization by BET, XRD, NMR, ICP, XAS, and TGA; and tables of XAS fitting results (PDF)

■ AUTHOR INFORMATION

Corresponding Author

Alexis T. Bell — Lawrence Berkeley National Laboratory, Berkeley, California 94720, United States; Department of Chemical and Biomolecular Engineering, University of California, Berkeley, California 94720, United States; orcid.org/0000-0002-5738-4645; Email: alexbell@berkeley.edu

Authors

Liang Qi — Lawrence Berkeley National Laboratory, Berkeley, California 94720, United States; Department of Chemical and Biomolecular Engineering, University of California, Berkeley, California 94720, United States

Melike Babucci — Department of Chemical Engineering, University of California, Davis, California 95616, United States; orcid.org/0000-0001-7785-3755

Yanfei Zhang — Lawrence Berkeley National Laboratory, Berkeley, California 94720, United States; Department of Chemical and Biomolecular Engineering, University of California, Berkeley, California 94720, United States

Alicia Lund — College of Chemistry, University of California, Berkeley, California 94720, United States

Lingmei Liu — Advanced Membranes and Porous Materials (AMPM) Center, Physical Sciences and Engineering Division, King Abdullah University of Science and Technology (KAUST), Thuwal 23955-6900, Saudi Arabia; Multi-scale Porous Materials Center, Institute of Advanced Interdisciplinary Studies & School of Chemistry and Chemical Engineering, Chongqing University, Chongqing 400044, China

Yizhen Chen — Department of Chemical Engineering, University of California, Davis, California 95616, United States

Adam S. Hoffman — Stanford Synchrotron Radiation Light Source, SLAC National Accelerator Laboratory, Menlo Park, California 94025, United States

Simon R. Bare — Stanford Synchrotron Radiation Light Source, SLAC National Accelerator Laboratory, Menlo Park, California 94025, United States

Yu Han – *Advanced Membranes and Porous Materials (AMPM) Center, Physical Sciences and Engineering Division, King Abdullah University of Science and Technology (KAUST), Thuwal 23955-6900, Saudi Arabia; KAUST Catalysis Center (KCC), KAUST, Thuwal 23955-6900, Saudi Arabia;* orcid.org/0000-0003-1462-1118

Bruce C. Gates – *Department of Chemical Engineering, University of California, Davis, California 95616, United States;* orcid.org/0000-0003-0274-4882

Complete contact information is available at:
<https://pubs.acs.org/10.1021/jacs.1c10261>

Notes

The authors declare no competing financial interest.

ACKNOWLEDGMENTS

This work was supported by the Office of Science, Office of Basic Energy Sciences (BES), of the U.S. Department of Energy (DOE) under Contract Nos. DE-AC02-05CH11231, DE-SC0012702 (an Energy Frontier Research Center, the Inorganometallic Catalyst Design Center, MB), and DE-FG02-04ER15513. L.Q. also acknowledges support from the Dalian Institute of Chemical Physics, Chinese Academy of Sciences, People's Republic of China. Use of the Stanford Synchrotron Radiation Light Source (SSRL), SLAC National Accelerator Laboratory, is supported by the DOE BES, under Contract No. DE-AC02-76SF00515. Additional support by the Consortium for Operando and Advanced Catalyst Characterization via Electronic Spectroscopy and Structure (Co-ACCESS) at SLAC is acknowledged. Co-ACCESS is supported by DOE, BES, Chemical Sciences, Geosciences and Biosciences, under Contract DE-AC02-76SF00515. We thank Dr. Hasan Celik and UC Berkeley's NMR facility in the College of Chemistry (CoC-NMR) for spectroscopic assistance. We thank Dr. Xinglong Dong of KAUST and Jia Lv of Chongqing University for assistance with STEM.

REFERENCES

- (1) Motagamwala, A. H.; Almallahi, R.; Wortman, J.; Igenegbai, V. O.; Lincic, S. Stable and selective catalysts for propane dehydrogenation operating at thermodynamic limit. *Science* **2021**, *373* (6551), 217–222.
- (2) Yan, H.; He, K.; Samek, I. A.; Jing, D.; Nanda, M. G.; Stair, P. C.; Notestein, J. M. Tandem In_2O_3 -Pt/ Al_2O_3 catalyst for coupling of propane dehydrogenation to selective H_2 combustion. *Science* **2021**, *371* (6535), 1257–1260.
- (3) Hannagan, R. T.; Giannakakis, G.; Réocreux, R.; Schumann, J.; Finzel, J.; Wang, Y.; Michaelides, A.; Deshlahra, P.; Christopher, P.; Flytzani-Stephanopoulos, M.; Stamatakis, M.; Sykes, E. C. H. First-principles design of a single-atom–alloy propane dehydrogenation catalyst. *Science* **2021**, *372* (6549), 1444–1447.
- (4) Ryoo, R.; Kim, J.; Jo, C.; Han, S. W.; Kim, J.-C.; Park, H.; Han, J.; Shin, H. S.; Shin, J. W. Rare-earth–platinum alloy nanoparticles in mesoporous zeolite for catalysis. *Nature* **2020**, *585* (7824), 221–224.
- (5) Grant, J. T.; Carrero, C. A.; Goeltl, F.; Venegas, J.; Mueller, P.; Burt, S. P.; Specht, S. E.; McDermott, W. P.; Chierigato, A.; Hermans, I. Selective oxidative dehydrogenation of propane to propene using boron nitride catalysts. *Science* **2016**, *354* (6319), 1570–1573.
- (6) Sattler, J. J. H. B.; Ruiz-Martinez, J.; Santillan-Jimenez, E.; Weckhuysen, B. M. Catalytic Dehydrogenation of Light Alkanes on Metals and Metal Oxides. *Chem. Rev.* **2014**, *114* (20), 10613–10653.
- (7) <https://www.ameriresearch.com/product/propylene-market-size-report/> (accessed 2021-10-29).
- (8) Sun, Q. M.; Wang, N.; Fan, Q. Y.; Zeng, L.; Mayoral, A.; Miao, S.; Yang, R. O.; Jiang, Z.; Zhou, W.; Zhang, J. C.; Zhang, T. J.; Xu, J.; Zhang, P.; Cheng, J.; Yang, D. C.; Jia, R.; Li, L.; Zhang, Q. H.; Wang, Y.;

Terasaki, O.; Yu, J. H. Subnanometer Bimetallic Platinum-Zinc Clusters in Zeolites for Propane Dehydrogenation. *Angew. Chem., Int. Ed.* **2020**, *59* (44), 19450–19459.

(9) Nakaya, Y.; Hirayama, J.; Yamazoe, S.; Shimizu, K. i.; Furukawa, S. Single-atom Pt in intermetallics as an ultrastable and selective catalyst for propane dehydrogenation. *Nat. Commun.* **2020**, *11* (1), 2838–2845.

(10) Chen, S.; Zhao, Z.-J.; Mu, R.; Chang, X.; Luo, J.; Purdy, S. C.; Kropf, A. J.; Sun, G.; Pei, C.; Miller, J. T.; et al. Propane Dehydrogenation on Single-Site [PtZn₄] Intermetallic Catalysts. *Chem.* **2021**, *7* (2), 387–405.

(11) Liu, L. C.; Lopez-Haro, M.; Lopes, C. W.; Li, C. G.; Concepcion, P.; Simonelli, L.; Calvino, J. J.; Corma, A. Regioselective generation and reactivity control of subnanometric platinum clusters in zeolites for high-temperature catalysis. *Nat. Mater.* **2019**, *18* (8), 866–873.

(12) Marcinkowski, M. D.; Darby, M. T.; Liu, J. L.; Wimple, J. M.; Lucci, F. R.; Lee, S.; Michaelides, A.; Flytzani-Stephanopoulos, M.; Stamatakis, M.; Sykes, E. C. H. Pt/Cu single-atom alloys as coke-resistant catalysts for efficient C-H activation. *Nat. Chem.* **2018**, *10* (3), 325–332.

(13) Liu, L. C.; Diaz, U.; Arenal, R.; Agostini, G.; Concepcion, P.; Corma, A. Generation of subnanometric platinum with high stability during transformation of a 2D zeolite into 3D. *Nat. Mater.* **2017**, *16* (1), 132–138.

(14) Cybulskis, V. J.; Bukowski, B. C.; Tseng, H. T.; Gallagher, J. R.; Wu, Z. W.; Wegener, E.; Kropf, A. J.; Ravel, B.; Ribeiro, F. H.; Greeley, J.; Miller, J. T. Zinc Promotion of Platinum for Catalytic Light Alkane Dehydrogenation: Insights into Geometric and Electronic Effects. *ACS Catal.* **2017**, *7* (6), 4173–4181.

(15) Wegener, E. C.; Bukowski, B. C.; Yang, D. L.; Wu, Z. W.; Kropf, A. J.; Delgass, W. N.; Greeley, J.; Zhang, G. H.; Miller, J. T. Intermetallic Compounds as an Alternative to Single-atom Alloy Catalysts: Geometric and Electronic Structures from Advanced X-ray Spectroscopies and Computational Studies. *ChemCatChem* **2020**, *12* (5), 1325–1333.

(16) Chen, S.; Pei, C.; Sun, G.; Zhao, Z.-J.; Gong, J. Nanostructured Catalysts toward Efficient Propane Dehydrogenation. *Acc. Mater. Res.* **2020**, *1*, 30–40.

(17) Zhang, Y. W.; Zhou, Y. M.; Shi, J. J.; Zhou, S. J.; Sheng, X. L.; Zhang, Z. W.; Xiang, S. M. Comparative study of bimetallic Pt-Sn catalysts supported on different supports for propane dehydrogenation. *J. Mol. Catal. A: Chem.* **2014**, *381*, 138–147.

(18) Wu, J.; Peng, Z. M.; Bell, A. T. Effects of composition and metal particle size on ethane dehydrogenation over $\text{Pt}_x\text{Sn}_{100-x}/\text{Mg}(\text{Al})\text{O}$ ($70 \leq x \leq 100$). *J. Catal.* **2014**, *311*, 161–168.

(19) Vajda, S.; Pellin, M. J.; Greeley, J. P.; Marshall, C. L.; Curtiss, L. A.; Ballentine, G. A.; Elam, J. W.; Catillon-Mucherie, S.; Redfern, P. C.; Mehmood, F.; Zapol, P. Subnanometer platinum clusters as highly active and selective catalysts for the oxidative dehydrogenation of propane. *Nat. Mater.* **2009**, *8* (3), 213–216.

(20) Liu, L.; Lopez-Haro, M.; Lopes, C. W.; Rojas-Buzo, S.; Concepcion, P.; Manzorro, R.; Simonelli, L.; Sattler, A.; Serna, P.; Calvino, J. J.; et al. Structural modulation and direct measurement of subnanometric bimetallic PtSn clusters confined in zeolites. *Nat. Catal.* **2020**, *3* (8), 628–638.

(21) Zhang, W.; Wang, H.; Jiang, J.; Sui, Z.; Zhu, Y.; Chen, D.; Zhou, X. Size Dependence of Pt Catalysts for Propane Dehydrogenation: from Atomically Dispersed to Nanoparticles. *ACS Catal.* **2020**, *10* (21), 12932–12942.

(22) Babucci, M.; Guntida, A.; Gates, B. C. Atomically Dispersed Metals on Well-Defined Supports including Zeolites and Metal–Organic Frameworks: Structure, Bonding, Reactivity, and Catalysis. *Chem. Rev.* **2020**, *120* (21), 11956–11985.

(23) Zhu, J.; Yang, M.-L.; Yu, Y.; Zhu, Y.-A.; Sui, Z.-J.; Zhou, X.-G.; Holmen, A.; Chen, D. Size-dependent reaction mechanism and kinetics for propane dehydrogenation over Pt catalysts. *ACS Catal.* **2015**, *5* (11), 6310–6319.

(24) Han, Z.; Li, S.; Jiang, F.; Wang, T.; Ma, X.; Gong, J. Propane dehydrogenation over Pt–Cu bimetallic catalysts: the nature of coke

deposition and the role of copper. *Nanoscale* **2014**, *6* (17), 10000–10008.

(25) Cai, W.; Mu, R.; Zha, S.; Sun, G.; Chen, S.; Zhao, Z.-J.; Li, H.; Tian, H.; Tang, Y.; Tao, F. F.; et al. Subsurface catalysis-mediated selectivity of dehydrogenation reaction. *Sci. Adv.* **2018**, *4* (8), eaar5418.

(26) Searles, K.; Chan, K. W.; Mendes Burak, J. A.; Zemlyanov, D.; Safonova, O.; Coperet, C. Highly Productive Propane Dehydrogenation Catalyst Using Silica-Supported Ga-Pt Nanoparticles Generated from Single-Sites. *J. Am. Chem. Soc.* **2018**, *140* (37), 11674–11679.

(27) Wegener, E. C.; Wu, Z.; Tseng, H.-T.; Gallagher, J. R.; Ren, Y.; Diaz, R. E.; Ribeiro, F. H.; Miller, J. T. Structure and reactivity of Pt–In intermetallic alloy nanoparticles: Highly selective catalysts for ethane dehydrogenation. *Catal. Today* **2018**, *299*, 146–153.

(28) Wu, Z.; Bukowski, B. C.; Li, Z.; Milligan, C.; Zhou, L.; Ma, T.; Wu, Y.; Ren, Y.; Ribeiro, F. H.; Delgass, W. N.; et al. Changes in catalytic and adsorptive properties of 2 nm Pt₃Mn nanoparticles by subsurface atoms. *J. Am. Chem. Soc.* **2018**, *140* (44), 14870–14877.

(29) Cesar, L. G.; Yang, C.; Lu, Z.; Ren, Y.; Zhang, G.; Miller, J. T. Identification of a Pt₃Co surface intermetallic alloy in Pt–Co propane dehydrogenation catalysts. *ACS Catal.* **2019**, *9* (6), 5231–5244.

(30) Zha, S.; Sun, G.; Wu, T.; Zhao, J.; Zhao, Z.-J.; Gong, J. Identification of Pt-based catalysts for propane dehydrogenation via a probability analysis. *Chem. Sci.* **2018**, *9* (16), 3925–3931.

(31) Xie, L.; Chai, Y.; Sun, L.; Dai, W.; Wu, G.; Guan, N.; Li, L. Optimizing zeolite stabilized Pt–Zn catalysts for propane dehydrogenation. *J. Energy Chem.* **2021**, *57*, 92–98.

(32) Wang, Y. S.; Hu, Z. P.; Lv, X. W.; Chen, L.; Yuan, Z. Y. Ultrasmall PtZn bimetallic nanoclusters encapsulated in silicalite-1 zeolite with superior performance for propane dehydrogenation. *J. Catal.* **2020**, *385*, 61–69.

(33) Rochlitz, L.; Searles, K.; Alfke, J.; Zemlyanov, D.; Safonova, O. V.; Copéret, C. Silica-supported, narrowly distributed, subnanometric Pt–Zn particles from single sites with high propane dehydrogenation performance. *Chem. Sci.* **2020**, *11* (6), 1549–1555.

(34) Hammond, C.; Conrad, S.; Hermans, I. Simple and scalable preparation of highly active lewis acidic Sn-β. *Angew. Chem., Int. Ed.* **2012**, *51* (47), 11736–11739.

(35) Qi, L.; Zhang, Y.; Conrad, M. A.; Russell, C. K.; Miller, J.; Bell, A. T. Ethanol Conversion to Butadiene over Isolated Zinc and Yttrium Sites Grafted onto Dealuminated Beta Zeolite. *J. Am. Chem. Soc.* **2020**, *142* (34), 14674–14687.

(36) Marques, J. P.; Gener, I.; Ayrault, P.; Bordado, J. C.; Lopes, J. M.; Ribeiro, F. R.; Guisnet, M. Dealumination of HBEA zeolite by steaming and acid leaching: distribution of the various aluminic species and identification of the hydroxyl groups. *C. R. Chim.* **2005**, *8* (3–4), 399–410.

(37) Rahman, I. A.; Padavettan, V. Synthesis of silica nanoparticles by sol-gel: size-dependent properties, surface modification, and applications in silica-polymer nanocomposites—A Review. *J. Nanomater.* **2012**, *2012*, 132424.

(38) Qasim, M.; Ananthaiah, J.; Dhara, S.; Paik, P.; Das, D. Synthesis and characterization of ultra-fine colloidal silica nanoparticles. *Adv. Sci., Eng. Med.* **2014**, *6* (9), 965–973.

(39) Wang, L.; Sang, S.; Meng, S.; Zhang, Y.; Qi, Y.; Liu, Z. Direct synthesis of Zn-ZSM-5 with novel morphology. *Mater. Lett.* **2007**, *61* (8–9), 1675–1678.

(40) Zhang, Y. W.; Zhou, Y. M.; Huang, L.; Zhou, S. J.; Sheng, X. L.; Wang, Q. L.; Zhang, C. Structure and catalytic properties of the Zn-modified ZSM-5 supported platinum catalyst for propane dehydrogenation. *Chem. Eng. J.* **2015**, *270*, 352–361.

(41) Chen, C.; Hu, Z. P.; Ren, J. T.; Zhang, S. M.; Wang, Z.; Yuan, Z. Y. ZnO Nanoclusters Supported on Dealuminated Zeolite beta as a Novel Catalyst for Direct Dehydrogenation of Propane to Propylene. *ChemCatChem* **2019**, *11* (2), 868–877.

(42) Li, Y.; Bu, Y.; Liu, Q.; Zhang, X.; Xu, J. High photocatalytic activities of zinc oxide nanotube arrays modified with tungsten trioxide nanoparticles. *Chin. J. Catal.* **2018**, *39* (1), 54–62.

(43) Gabrienko, A. A.; Arzumanov, S. S.; Toktarev, A. V.; Danilova, I. G.; Prosvirnin, I. P.; Kriventsov, V. V.; Zaikovskii, V. I.; Freude, D.;

Stepanov, A. G. Different efficiency of Zn²⁺ and ZnO species for methane activation on Zn-modified zeolite. *ACS Catal.* **2017**, *7* (3), 1818–1830.

(44) Ruiz, M. G.; Casados, D. A. S.; Pliego, J. A.; Álvarez, C. M.; de Andrés, E. S.; Tartalo, D. S.; Vaque, R. S.; Casas, M. G. ZSM-5 zeolites modified with Zn and their effect on the crystal size in the conversion of methanol to light aromatics (MTA). *React. Kinet., Mech. Catal.* **2020**, *129* (1), 471–490.

(45) Yan, W.; Xi, S.; Du, Y.; Schreyer, M. K.; Tan, S. X.; Liu, Y.; Borgna, A. Heteroatomic Zn-MWW Zeolite Developed for Catalytic Dehydrogenation Reactions: A Combined Experimental and DFT Study. *ChemCatChem* **2018**, *10* (14), 3078–3085.

(46) Cambor, M. A.; Davis, M. E. ²⁹Si MAS NMR spectroscopy of tecto-zincosilicates. *J. Phys. Chem.* **1994**, *98* (50), 13151–13156.

(47) Qi, G.; Wang, Q.; Xu, J.; Trébosc, J.; Lafon, O.; Wang, C.; Amoureux, J. P.; Deng, F. Synergic Effect of Active Sites in Zinc-Modified ZSM-5 Zeolites as Revealed by High-Field Solid-State NMR Spectroscopy. *Angew. Chem., Int. Ed.* **2016**, *128* (51), 16058–16062.

(48) Wang, X.-J.; Jaye, C.; Nam, K.-W.; Zhang, B.; Chen, H.-Y.; Bai, J.; Li, H.; Huang, X.; Fischer, D. A.; Yang, X.-Q. Investigation of the structural changes in Li_{1-x}FePO₄ upon charging by synchrotron radiation techniques. *J. Mater. Chem.* **2011**, *21* (30), 11406–11411.

(49) Bus, E.; Prins, R.; van Bokhoven, J. A. Time-resolved in situ XAS study of the preparation of supported gold clusters. *Phys. Chem. Chem. Phys.* **2007**, *9* (25), 3312–3320.

(50) Yoon, W.-S.; Chung, K. Y.; McBreen, J.; Zaghbi, K.; Yang, X.-Q. Electronic Structure of the Electrochemically Delithiated Li_{1-x}FePO₄ Electrodes Investigated by P K-edge X-Ray Absorption Spectroscopy. *Electrochem. Solid-State Lett.* **2006**, *9* (9), A415–A417.

(51) Freitag, K.; Molon, M.; Jerabek, P.; Dilchert, K.; Rösler, C.; Seidel, R. W.; Gemel, C.; Frenking, G.; Fischer, R. A. Zn···Zn interactions at nickel and palladium centers. *Chem. Sci.* **2016**, *7* (10), 6413–6421.

(52) Bortnovsky, O.; Sobalik, Z.; Wichterlová, B. Exchange of Co (II) ions in H-BEA zeolites: identification of aluminum pairs in the zeolite framework. *Microporous Mesoporous Mater.* **2001**, *46* (2–3), 265–275.

(53) Dědeček, J.; Tabor, E.; Sklenak, S. Tuning the aluminum distribution in zeolites to increase their performance in acid-catalyzed reactions. *ChemSusChem* **2019**, *12* (3), 556–576.

(54) Kim, J.; Jentys, A.; Maier, S. M.; Lercher, J. A. Characterization of Fe-exchanged BEA zeolite under NH₃ selective catalytic reduction conditions. *J. Phys. Chem. C* **2013**, *117* (2), 986–993.

(55) Hauser, A. W.; Horn, P. R.; Head-Gordon, M.; Bell, A. T. A systematic study on Pt based, subnanometer-sized alloy cluster catalysts for alkane dehydrogenation: effects of intermetallic interaction. *Phys. Chem. Chem. Phys.* **2016**, *18* (16), 10906–10917.

(56) Chang, Q.-Y.; Yin, Q.; Ma, F.; Zhu, Y.-A.; Sui, Z.-J.; Zhou, X.-G.; Chen, D.; Yuan, W.-K. Tuning adsorption and catalytic properties of α-Cr₂O₃ and ZnO in propane dehydrogenation by creating oxygen vacancy and doping single Pt atom: a comparative first-principles study. *Ind. Eng. Chem. Res.* **2019**, *58* (24), 10199–10209.

(57) Saerens, S.; Sabbe, M. K.; Galvita, V. V.; Redekop, E. A.; Reyniers, M. F.; Marin, G. B. The positive role of hydrogen on the dehydrogenation of propane on Pt (111). *ACS Catal.* **2017**, *7* (11), 7495–7508.

(58) Campbell, C. T. Bimetallic surface chemistry. *Annu. Rev. Phys. Chem.* **1990**, *41*, 775–837.

(59) Massiot, D.; Fayon, F.; Capron, M.; King, I.; Le Calvé, S.; Alonso, B.; Durand, J. O.; Bujoli, B.; Gan, Z.; Hoatson, G. Modelling one- and two-dimensional solid-state NMR spectra. *Magn. Reson. Chem.* **2002**, *40* (1), 70–76.

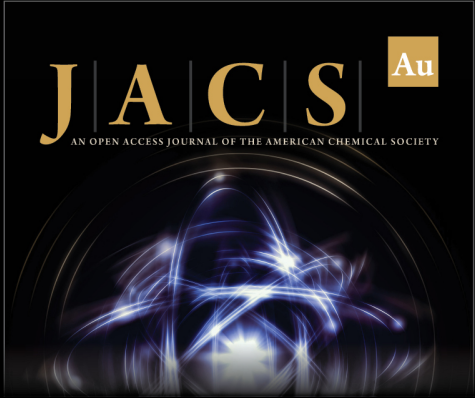
(60) Hoffman, A. S.; Singh, J. A.; Bent, S. F.; Bare, S. R. In situ observation of phase changes of a silica-supported cobalt catalyst for the Fischer–Tropsch process by the development of a synchrotron-compatible in situ/operando powder X-ray diffraction cell. *J. Synchrotron Radiat.* **2018**, *25* (6), 1673–1682.

(61) Ravel, B.; Newville, M. ATHENA, ARTEMIS, HEPHAESTUS: data analysis for X-ray absorption spectroscopy using IFEFFIT. *J. Synchrotron Radiat.* **2005**, *12* (4), 537–541.


(62) Lytle, F. Report of the international workshop on standard and criteria in x-ray absorption spectroscopy. *Phys. B* **1989**, *158*, 701–722.


(63) Newville, M. Larch: an analysis package for XAFS and related spectroscopies. *J. Phys.: Conf. Ser.* **2013**, *430*, 012007.


(64) Munoz, M.; Argoul, P.; Farges, F. Continuous Cauchy wavelet transform analyses of EXAFS spectra: A qualitative approach. *Am. Mineral.* **2003**, *88* (4), 694–700.



JACS Au
AN OPEN ACCESS JOURNAL OF THE AMERICAN CHEMICAL SOCIETY

 Editor-in-Chief
Prof. Christopher W. Jones
Georgia Institute of Technology, USA

Open for Submissions 

pubs.acs.org/jacsau  ACS Publications
Most Trusted. Most Cited. Most Read.